Automated identification of local contamination in remote atmospheric composition time series

Ivo Beck[1], Hélène Angot[1], Andrea Baccarini[1], Lubna Dada[1], Lauriane Quéléver[2], Tuija Jokinen[2,3], Tiia Laurila[2], Markus Lampimäki[2], Nicolas Bukowiecki[4], Matthew Boyer[2], Xianda Gong[5], Martin Gysel-Beer[6], Tuukka Petäjä[2], Jian Wang[5], and Julia Schmale[1*]

[1]Extreme Environments Research Laboratory, École Polytechnique fédérale de Lausanne, Switzerland
[2]Institute for Atmospheric and Earth System Research, INAR/Physics, FI-00014 University of Helsinki, Finland
[3]Climate & Atmosphere Research Centre (CARE-C), The Cyprus Institute, P.O. Box 27456, Nicosia, 1645, Cyprus
[4] Atmospheric Sciences, Department of Environmental Sciences, University of Basel, Switzerland
[5]Center for Aerosol Science and Engineering, Department of Energy, Environmental and Chemical Engineering, Washington University in St. Louis, St. Louis, MO, USA
[6]Laboratory of Atmospheric Chemistry, Paul Scherrer Institute, Villigen PSI, Switzerland
*Correspondence to: Julia Schmale (julia.schmale@epfl.ch), Ivo Beck (ivo.beck@epfl.ch)

Abstract.

Atmospheric observations in remote locations offer a possibility to explore trace gas and particle concentrations in pristine environments. However, data from remote areas are often contaminated by pollution from local sources. Detecting this ~~pollution~~contamination is thus a central and frequently encountered issue. Consequently, many different methods exist today to identify local ~~pollution~~contamination in atmospheric composition measurement time series, but no single method has been widely accepted. In this study, we present a new method to identify primary pollution in remote atmospheric datasets, e.g., from ship campaigns or stations with low background signal compared to the ~~pollution~~ contaminated signal. The Pollution Detection Algorithm (PDA) identifies and flags periods of polluted data in five steps. The first and most important step identifies polluted periods based on the ~~gradient~~derivative (time-derivative) of a concentration over time. If this ~~gradient~~derivative exceeds a given threshold, data are flagged as polluted. Further pollution identification steps are a simple concentration threshold filter, a neighboring points filter (optional), a median and a sparse data filter (optional). The PDA only relies on the target dataset itself and is independent of ancillary datasets such as meteorological variables. All parameters of each step are adjustable so that the PDA can be "tuned" to be more or less stringent (e.g., flag more or less data points as ~~polluted~~contaminated).

The PDA was developed and tested with a particle number concentration dataset collected during the Multidisciplinary drifting Observatory for the Study of Arctic Climate (MOSAiC) expedition in the Central Arctic. Using strict settings, we identified 62 % of the data as influenced by local ~~pollution~~contamination. Using a second independent particle number concentration dataset also collected during MOSAiC, we evaluated the performance of the PDA against the same dataset cleaned by visual inspection. The two methods agreed in 94 % of the cases. Additionally, the PDA was successfully applied on a trace gas dataset (CO_2), also collected during MOSAiC, and on another particle number concentration dataset, collected at the high altitude background station Jungfraujoch, Switzerland. Thus, the PDA proves to be a useful and flexible tool to identify periods affected by local ~~pollution~~contamination in atmospheric composition datasets without the need for ancillary measurements. It is best applied to data representing primary pollution. The user-friendly and open access code enables reproducible application to a wide suite of different datasets. It is available at: https://doi.org/10.5281/zenodo.5761101.

1 Introduction

Aerosol and trace gas measurements in remote environments, such as polar or high altitude regions, are essential to improve our understanding of key climate and biogeochemical processes and to constrain numerical models (Carslaw et al., 2010; Bukowiecki et al., 2016; Reddington et al., 2017). A major challenge associated with obtaining atmospheric composition measurements in such locations is that data are often impacted by emissions from local activities, which are not representative of the remote environment and interfere with the observation and data analysis objectives (Bukowiecki et al., 2021). Such local pollution emissions can originate from the measurement platform itself, e.g., research vessels (Schmale et al., 2019; Baccarini et al., 2020; Humphries et al., 2016), or from touristic (Bukowiecki et al., 2021), local anthropogenic (Asmi et al., 2016) or

nearby industrial (Kolesar et al., 2017) activities. Local emissions often originate from combustion processes and can directly affect trace gas mixing ratios (hereafter referred to as concentrations), aerosol concentrations, and other particle properties. For subsequent analysis, the influence of local ~~pollution~~contamination must be correctly detected to separate polluted from unaffected data. Local ~~pollution~~contamination influence is typically characterized by enhanced particle or trace gas concentrations and strong variations in the signal amplitude on time scales varying between a few seconds (Bukowiecki et al., 2021; Baccarini et al., 2020) to several hours, depending on the nature of the emitting activity and wind direction. Pollution "spikes" disturb the measurement of the regional or remote background concentrations, which are inherently continuous and vary over time due to meteorological factors such as the boundary layer evolution (Bukowiecki et al., 2021), synoptic situations (Alroe et al., 2020) or relatively slow natural processes such as marine biogenic emissions (Frossard et al., 2014) or sea ice related new particle formation (Baccarini et al., 2020).

Numerous atmospheric composition measurements have been conducted in remote environments, such as the Arctic (Leck et al., 1996; Uttal et al., 2002; Tjernström et al., 2014) and the Southern Ocean (McFarquhar et al., 2021; Schmale et al., 2019), or at regional background sites around the Arctic (Uttal et al., 2016; Freud et al., 2017) or throughout Europe as part of the established monitoring network Aerosols, Clouds, and Trace gases Research Infrastructure (ACTRIS) (Herrmann et al., 2015; Asmi et al., 2013; Bukowiecki et al., 2021). Different approaches have been applied to detect and remove polluted data from ~~these~~ a large variety of measurement sites. We provide a short overview here.

In one approach, Herrmann et al. (2015) removed polluted data based on visual inspection of the submicron particle size distribution spectra. Other approaches are based on the application of statistical filters that identify ~~pollution~~contamination based on outliers that deviate from a curve fitted to the data. Bukowiecki et al. (2002) developed a method for aerosols based on the 5th percentile within each minute, assuming it reflects uncontaminated background concentrations. This method has the caveat that for times without contamination, the background is biased low, while for highly contaminated data, the background is biased high. Ruckstuhl et al. (2012) assumed that a trace gas background signal is a combination of a baseline signal with the contribution of pollution. The background signal is estimated by applying a linear regression. The outliers are detected as the data points that exceed the estimated background by a factor of 3σ. This method is called 'robust extraction of baseline signal' (REBS). El Yazidi et al. (2018) applied the REBS method to four datasets of trace gas measurements and compared it to the standard deviation method for particles (Drewnick et al., 2012), which detects ~~pollution~~contamination as data points that differ by more than 3σ from the median of the data, and to the coefficient of variation (COV) method (Hagler et al., 2012), which uses the 99th percentile of the COV as a threshold for contamination. Hereby, the COV is defined as the standard deviation of a moving time window (5 min), divided by the mean value of the whole dataset. Brantley et al. (2014) compared a standard deviation-based method to the COV method to detect exhaust plumes from air quality measurements on a road. Both these methods work for datasets in which the signal of plumes is characterized by high variability and magnitude (Brantley et al., 2014). McNabola et al. (2011) applied baseflow separation techniques, such as low pass filters, or moving interval filters, known from stream-flow hydrology, to separate background concentrations in urban PM10 measurements and compared the result to background PM10 measurements. Gallo et al., (2020) developed a method to retrieve the regional

aerosol number concentration baseline at the Eastern North Atlantic (ENA) Atmospheric Radiation Measurement (ARM) user facility from the U.S. Department of Energy's (DOE). The ENA Aerosol Mask (ENA-AM) identifies data points, which exceed the standard deviation of the data below the median (σ_b) of a 1- month period by more than a factor α. They found the method to work best for time periods between two weeks and one month, and less than half of the data points influenced by local contamination. Liu et al. (2018), used a de-spike algorithm, based on a 24 h running median window, to remove short-term local contamination events of less than 1h duration from an aerosol time series measured at McMurdo Station in Antarctica. Giostra et al. (2011) used a statistical approach where they extract the baseline with a decomposition of the probability density function of the data. Polluted data shows a gamma distribution, the baseline is represented as a Gaussian distribution. This method was applied on halocarbon data from remote marine or alpine stations. Most recently, Bukowiecki et al. (2021) developed a new spike detection method for regional background observations. First, a signal baseline was determined for the 1-min total particle number concentration data based on a running 5th percentile, with an optimized time window and percentile threshold. This baseline was then subtracted from the original time series to isolate spikes in the time series. Finally, a spike flag was applied by removing data when the 1-min spike time series exceeded the 80th percentile of the surrounding 1-h time window by a user-defined fixed threshold. Generally, such statistical methods are not suited to reveal background signals at times when they are dominated by non-background signals, because this carries a risk that the non-background signals are falsely included in the background signals (Ruckstuhl et al., 2012).

Another commonly used pollution filtering method is based on wind direction. In this case, a pollutioncontamination source sector can be defined to flag all time periods in a dataset with wind coming from this sector; winds from outside the source sector are assumed to be pollutioncontamination free (Leck et al., 1996; Asmi et al., 2016; Kyrö et al., 2013). For the Arctic Summer Cloud Ocean Study in 2008 on the Swedish icebreaker Oden, the measurement of a pollution tracer (toluene) was used in addition to a wind filter. If the toluene concentration running mean exceeded a threshold, the data were flagged as polluted (Tjernström et al., 2014). Toluene concentration measurements require complex instrumentation and are therefore not routinely observed. An inherent limitation of wind filters is that they cannot take into account the effect of recirculation of the emitted pollution, which can lead to contaminated measurements from different wind sectors. Humphries et al. (2019) used a combination of a carbon monoxide (CO) concentration threshold with a statistical filter applied to carbon dioxide (CO_2) and black carbon (BC) data to clean particle number concentration and cloud condensation nuclei datasets. Data were collected on the Australian research vessel *Investigator* in 2016 in the Tasman Sea. The statistical filter flags the data points that deviate from the 5-min mean of each variable by a certain threshold. Additionally, a window filter was applied that sums all data points in a 20 min time window. If the sum of the polluted data points surpassed 10 % of the data points in the time window in one of the three datasets (CO, CO_2 or BC), all data points within this time window were flagged as polluted. Similarly, Schmale et al. (2019) and Moallemi et al. (2021) used a combination of CO_2 and particle number concentration data to detect contamination from ship exhaust. A binomial smoothing was applied to each time series, and when the ratio of the smoothed data over the original time series exceeded certain thresholds, the data were flagged as polluted.

The above examples demonstrate that there are many different ways of detecting local ~~pollution~~contamination in a dataset and
that no single method has established itself and is widely used. While custom-made methods have the advantage that they are
designed to work particularly well for a specific dataset, they have the disadvantage that they cannot necessarily be applied to
other datasets, because they rely on ancillary information that might not be readily available at all measurement sites. This
means that pollution-detection methods are not always reproducible and make comparison between cleaned datasets more
challenging. Therefore, a common filtering method, which relies on a minimal number of input variables, is desirable to
achieve reproducible pollution detection across a variety of datasets.

Here, we propose an algorithm to clean up particle number concentrations, particle number size distribution and trace gas
concentration datasets collected at remote or background sites that experience random influence from local primary pollution
sources. This method only requires a time series of the target particle number or trace gas concentration data and is independent
of ancillary datasets such as BC or meteorological variables. As a result, the method can be applied to a large number of
measurement sites. ~~We embedded the algorithm in a user friendly python based code.~~ The algorithm detects ~~polluted~~
contaminated periods in five steps. To increase the usability of this algorithm, the parameters can be "tuned" to adapt to
different datasets, ambient conditions and requirements. This makes the algorithm an efficient and consistent way to detect
local contamination in large remote atmospheric time series, as they exist for example from ship campaigns or from remote
stations. This method is objective as the treatment of the data is consistent throughout the whole time series considered, because
the same value of each parameter is applied to the entire dataset.

After introducing the PDA in detail in the methods, we evaluate its performance in the results section in three steps. First, the
general evaluation is based on particle number concentration data measured during the MOSAiC expedition (Multidisciplinary
drifting Observatory for the Study of Arctic Climate) between September 2019 and October 2020 (Shupe et al., under review).
Second, we test results from the PDA against other common pollution identifying methods. Third, we evaluate its applicability
to further ship-based datasets such as aerosol number size distributions, aerosol mass composition, and trace gases
concentrations, as well as to a particle number concentration dataset from a high altitude observatory. We also provide an open
source, python-based, tool for download on zenodo (https://doi.org/10.5281/zenodo.5761101), including a manual, which
allows users to apply the same method to other datasets.

2 Methods

In this manuscript, we use the terms "contamination" and "pollution" interchangeably to describe local contamination. We
define local contamination as fresh exhaust plumes from the ship, skidoos, snow groomers and other local, anthropogenic
sources of pollution. We define the background concentration as unaffected from local contamination ~~and~~but well-mixed
ambient concentrations. This means that background observations can contain aged pollution, ~~instance~~ e.g. an aged plume
which is long-range transported to Polarstern (Dada et al., 2022). Note, that the aim of the PDA is to identify fresh local
contamination and we do not aim at detecting aged, well-mixed contamination. In this section, we first present the datasets

5

and instruments used for this study. In Sect. 2.2 and 2.3., we describe alternative filtering methods used to test the performance of the PDA. In Sect. 2.4., we describe the PDA with each of the five filtering steps in a dedicated subsection.

We developed and tested the PDA using atmospheric aerosol and trace gas concentrations measured in the *Swiss Container*
150 during the year-long MOSAiC expedition in the central Arctic. The expedition started in September 2019 in Tromsø, Norway and ended in October 2020 in Bremerhaven, Germany, whereby the Research Vessel (RV) *Polarstern* (Alfred-Wegener-Institut Helmholtz-Zentrum für Polar- und Meeresforschung, 2017) drifted with sea ice in the central Arctic Ocean. The drift track is shown in Fig. A1. The aim of the expedition was to study sea ice, ecological, biogeochemical, ocean and atmospheric processes in the Arctic Ocean. A research camp was set up on the ice around the ship. A comprehensive introduction to the
155 atmospheric measurements carried out during the expedition is presented in Shupe et. al. (under review). The *Swiss Container* was placed on the D-deck of the ship (see Fig. A2) to monitor the aerosol and gas phase atmospheric composition. Aerosols and trace gases were sampled from two different inlets: (i) a whole air inlet (total inlet) which allowed sampling all particles and droplets up to 40 µm and (ii) an interstitial inlet equipped with a cyclone to cut off particles larger than 1 µm, designed to sample particles that do not activate in cloud and fog (Fig. A3). The total inlet was built after the Global Atmosphere Watch
160 recommendations (World Meteorological Organization, 2016). An automated valve inside the container switched hourly between the total and interstitial inlets to allow instruments connected behind the valve to sample from each of the inlets alternately. The measurement setup and the instrumentation used during the expedition are shown in appendix A in Fig. A3. The flow of the inlets was kept constant at 10 (total inlet) and 16.7 L/min (interstitial inlet). The inlets above the container had a length of 1.5 m and sampled at a height of approximately 15 m above sea level. The temperature inside the *Swiss Container*
165 was kept constant at 20°C. The sampled air was dried when entering the container due to the strong temperature gradient between outside and inside, but additional inline heating was applied when necessary. Relative humidity (RH) in the inlet lines was continuously measured and maintained below 40 %.

Aerosol and trace gas measurements were regularly impacted by a variety of local pollution sources (e.g., ship stack, snow groomers, diesel generators, helicopters, ship vents). Polluted periods varied in time from seconds up to hours or days and the
170 intensity of contamination varied with the distance from and type of source and with the wind direction, wind speed and turbulent air motion around the ship.

To segregate polluted from unaffected data for final analysis, we developed an algorithm that detects and tags polluted periods independent of the pollution source's position relative to the measurement site. For the development of the PDA, we used a particle number concentration dataset. In the following subsections, we describe the methodology used to develop and evaluate
175 the performance of the PDA.

2.1 Instruments and data

2.1.1 Particle number concentration data

We used a particle number concentration dataset collected with a condensation particle counter (CPC) model 3025 by TSI (referred to as CPC3025) to develop the PDA. The CPC3025 has a minimum detectable particle diameter (50% counting efficiency) of $D_{p\_50} = 3$ nm and a maximum detectable particle concentration of $9.99*10^4$ cm^{-3}. It collected data at 10 s intervals during the expedition. The instrument was connected to the interstitial inlet. The sample flow of the CPC was set to 0.3 L/min during the entire expedition and was checked daily. We performed weekly zero tests with High Efficiency Particulate Air (HEPA) filters.

In addition to the CPC3025, we used particle number concentration data from the Aerosol Observing System (AOS) to evaluate the performance of the PDA. It was operated as part of the United States Department of Energy Atmospheric Radiation Measurement (ARM) facility during the same expedition. The ARM AOSs are measurement containers capable of measuring a suite of aerosol microphysical and chemical properties in a standardized, field-deployable design. Only a brief summary of the AOS is given here; a more comprehensive overview of the ARM AOS design, instrumentation, deployment history, and measurement objectives for the different facilities can be found in Uin et al. (2019).

The AOS was also located on the D-deck, at the port side of the *Swiss Container*, 2 m away (see Fig. A2). The aerosol instrumentation inside the AOS sampled from a single, shared total aerosol inlet on top of the AOS container. The inlet itself was 5 m in length, the inlet height was approximately 18 m above sea level. The particle number concentration data in the AOS container was obtained from a CPC model 3772 from TSI (referred to as CPCf) with a minimum detectable particle diameter of $D_{p\_50} = 10$ nm (Kuang et al., 2021). It ran with a flow rate of 1 L/min, and a sampling resolution of 1 second. The air to the CPC was dried before sampling using a Nafion dryer. Weekly filter tests and daily flow rate checks were performed. The temperature inside the AOS was maintained between 18-22°C. The AOS inlet was equipped with a purge blower that was designed specifically for this campaign to prevent ship stack pollution from entering the instruments. The purge blower was set up to trigger automatically according to elevated carbon monoxide (CO) concentrations, which were measured from a separate sample line that was collocated with the aerosol inlet. The purge blower was able to provide a high flow rate of continuous particle-free air into the AOS inlet, effectively purging the inlet of ship stack pollution. However, due to relatively low sensitivity of CO concentrations to pollution from the ship stack plume (see Fig. A4), the automated triggering system did not work automatically as planned. Thus, the purge blower was turned on manually when the bow of the ship was exposed to pollution for extended periods of time. As a result, the ARM CPC datasets show periodic gaps during local pollution events, but there are still times when the datasets are influenced by local ~~pollution~~contamination and additional cleaning is required. Therefore, the ARM CPC datasets are well suited to test the performance of the PDA.

To test the broader applicability of the PDA to datasets from sites with different characteristics, we used a particle number concentration dataset collected at the high-altitude GAW and ACTRIS research station Jungfraujoch (JFJ) in the Swiss Alps (Bukowiecki et al., 2016). The station is located at 3580 m.a.s.l. In winter it often represents the remote European free

troposphere, while in warmer seasons, intrusions of boundary layer air masses are frequently observed (Herrmann et al., 2015). The site also is a touristic destination, meaning that local ~~pollution~~contamination affecting the measurements interferes with the aim to achieve unpolluted background measurements (Bukowiecki et al., 2021). Data were collected by a CPC model 3772 by TSI. The measurement setup is described in more detail by (Bukowiecki et al., 2021). The results of this application are presented in Sect. 3.4.4.

2.1.2 Description of particle number concentration characteristics

During MOSAiC, local contamination occasionally originated from other sources than the stack, such as helicopters, snow groomers and snowmobiles, as well as small diesel generators on the ice. Therefore, the algorithm needs to detect contamination from different sources and directions. Figure 1 shows the whole dataset of minute-averaged particle number concentrations, as a function of the relative wind direction. Note that we used this particle number concentration dataset to develop the PDA. The stack is located at 180° from the bow and is marked as a grey vertical line in the figure. The majority of high concentration events ($>10^4$ cm^{-3}) are related to emissions from the stack, but there were occasions where high concentrations came from different directions. We define high concentrations as $> 10^4$ cm^{-3} because empirically we did not find any situation where the particle number concentration would increase to such high values in the Arctic without involvement of expedition-related activities (see Sect. 2.3.1). In contrast, we find low particle number concentrations of < 100 cm^{-3} for almost all wind directions, including from the stack direction. A stable and very low boundary layer occasionally avoided the polluted air from the stack to down-mix to the inlets of the *Swiss Container* so that the measurements remained unaffected by it despite the air coming directly from the exhaust (this is illustrated in the picture in Fig. A5). This makes it difficult to apply a simple, but commonly-used (Leck et al., 1996; Cox et al., 2003) filter based on wind direction. In addition, introducing a maximum concentration as a single threshold below which data are considered clean is not feasible, because natural particle concentrations vary across several orders of magnitude (Fig. 1). Pollution influence can also occasionally be so small that it would not surpass the threshold, e.g., when it is on the order of hundreds of particles on top of a low (e.g., $<$ 100 cm^{-3}) natural concentration (background concentration).

Generally, concentration data from remote regions, characterized by the absence of dominant local (anthropogenic) sources, vary only slowly with time, compared to when influenced by local contamination. This means that the concentration gradient (time derivative) is small. In contrast, concentration data show distinct variations, such as rapid fluctuations, when affected by contamination from nearby sources (e.g., Fig. A4). The PDA builds on this abrupt variation in concentration and detects polluted data based on the rate and magnitude of change in the concentration signal over a given time period. The basic principle of the PDA was developed and used for the 2018 Microbiology-Ocean-Cloud-Coupling in the High Arctic (MOCCHA) campaign on the Swedish ice breaker *Oden* by Baccarini (2021). Here, we further develop this algorithm and test it against different datasets. Importantly, the algorithm is only based on target concentration data and does not rely on ancillary datasets, such as particle size distribution or meteorological variables.

2.1.2 3 Particle number size distribution data

Furthermore, we applied the PDA to a particle size distribution dataset collected by a Scanning Mobility Particle Sizer (SMPS). The custom built SMPS (Schmale et al., 2017) was located in the *Swiss Container* behind the switching valve and recorded the size distribution of particles between 17 and 600 nm with a time resolution of three minutes. We applied the PDA to the SMPS integrated particle number concentration. The results are presented in Sect. 3.1.2.

2.1.3 4 Aerosol chemical composition data

In addition, we tested the performance of the PDA against the aerosol chemical composition dataset obtained by the High-Resolution Time-of-Flight Aerosol Mass Spectrometer (HR-ToF-AMS) from Aerodyne Research Inc., located in the *Swiss Container*. The AMS measures the chemical composition of non-refractory aerosols, i.e., species that evaporate at temperatures up to 600°C. It typically detects sulphate (SO_4^{2-}), nitrate (NO_3^-), ammonium (NH_4^+), chloride (Cl^-), and organics (DeCarlo et al., 2006) from particles in the size range 0.07 – 1 µm, defined by the type of aerodynamic lens. The AMS was operated behind the switching valve to sample both interstitial and total inlet aerosol populations. Here, we use the mass signal of the ion fragment $C_4H_9^+$ at a mass to charge ratio of m/z = 57. This fragment is a typical indicator of fresh fossil fuel combustion (Enroth et al., 2016; Massoli et al., 2012) and has been used before to detect ~~pollution~~contamination in remote regions (Schmale et al., 2013). The results of the application of the PDA on the chemical composition data will be discussed in Sect. 3.4.2.

2.1.4 5 Trace gas data

We also used trace gas data collected in the *Swiss Container* to test the algorithm on datasets other than particle number concentration (Sect. 3.4.3). A detailed description of trace gas measurements during the MOSAiC expedition is given in Angot et al. (in prep.). Briefly, carbon dioxide (CO_2), methane (CH_4), and CO ambient air mixing ratios were monitored by cavity ring-down spectroscopy using a Picarro instrument (model G2401) behind the interstitial inlet. Regular calibrations were carried out during the expedition with gas mixtures of known CO_2, CH_4 and CO mixing ratios. As described in Angot et al. (in prep.), nitric oxide (NO) ambient air concentrations were measured in a different container (University of Colorado) with a custom-built single-channel chemiluminescence analyzer (Fontijn et al., 1970), which was regularly calibrated by dynamic dilution of a 1.5 ppm compressed NO gas standard.

2.1.5 6 Wind data

Wind speed and direction were measured with a 2D sonic anemometer on the main mast of RV *Polarstern*. We used this wind dataset at a time resolution of 1 minute in this study (Schmithuesen, 2021a, b, c, d, e).

2.2 Wind based filtering method

270 The main source of local pollution during the MOSAiC expedition was the stack of the ship. Based on Fig. 1, it is possible to define a polluted wind sector from 90 - 270° relative to the bow of the ship. The wind-based filter flags all data points collected when the relative wind direction was coming from the polluted sector. This wind filter is introduced here for comparative purposes only. The comparison of the wind-based filtering method to the PDA is presented in Sect. 3.2.1.

2.3 Visual filtering method

275 The following visual filtering method is introduced here for comparative purposes: Every pollution filtering method contains a certain level of subjectivity since the final decision about polluted vs non-polluted must be made by the user. Therefore, we compared the performance of the PDA to the result of a visual-only filtering method, which was applied to the dataset of the CPCf. Impact from local ~~pollution~~contamination is often evident from the time series of pollution-related variables, such as wind direction, wind speed, total particle number concentration, one standard deviation of particle number concentration within 280 one minute periods (N_{std_1m}), and particle number size distribution. Time series of these variables were visually inspected for each day to identify the periods impacted by the local ~~pollution~~contamination. N_{std_1m} was used as the core feature of pollution influence. In periods unaffected by pollution, it was below 30 cm^{-3}. When the total particle number concentration was higher than ~600 cm^{-3} (such as during new particle formation events in the summertime, or during Arctic haze events in the wintertime), N_{std_1m} often increased to between 30 to 100 cm^{-3}. However, these periods were not treated as local 285 ~~pollution~~contamination influenced. Data were flagged as polluted when N_{std_1m} was above 10^3 cm^{-3}, the Aitken mode particle (i.e. diameter below 100 nm) number concentration was greatly enhanced and wind was coming from the stack direction. Periods moderately influenced by the local ~~pollution~~contamination, during which N_{std_1m} was typically between 10^2 to 10^3 cm^{-3} and the wind direction was usually not directly from the stack direction, are also flagged in this dataset. The visual filtering method also considered spikes and neighboring points. A spike of N_{std_1m} was defined as a point having a value that was 2 290 times higher than the 5-min moving average of N_{std_1m}. When two polluted flags were within 5-min of each other, all data points in between were flagged as polluted.

2.4 Pollution detection algorithm (PDA)

~~During MOSAiC, local pollution occasionally originated from other sources than the stack, such as helicopters, snow groomers and snowmobiles, as well as small diesel generators on the ice. Therefore, the algorithm needs to detect pollution from different~~ 295 ~~sources and directions. Figure 1 shows the whole dataset of minute-averaged particle number concentrations, as a function of the relative wind direction. Note that we used this particle number concentration dataset to develop the PDA. The stack is located at 180° from the bow and is marked as a grey vertical line in the figure. The majority of high concentration events (>10^4 cm^{-3}) are related to emissions from the stack, but there were occasions where high concentrations came from different directions. We define high concentrations as > 10^4 cm^{-3} because empirically we did not find any situation where the particle~~

10

300 ~~number concentration would increase to such high values in the Arctic without involvement of expedition-related activities (see Sect. 2.3.1). In contrast, we find low particle number concentrations of < 100 cm^{-3} for almost all wind directions, including from the stack direction. A stable and very low boundary layer occasionally avoided the polluted air from the stack to down-~~

305 ~~mix to the inlets of the *Swiss Container* so that the measurements remained unaffected by it despite the air coming directly from the exhaust (this is illustrated in the picture in Fig. A5). This makes it difficult to apply a simple, but commonly used (Leck et al., 1996; Cox et al., 2003) filter based on wind direction. In addition, introducing a maximum concentration as a single threshold below which data are considered clean is not feasible, because natural particle concentrations vary across several orders of magnitude (Fig. 1). Pollution influence can also occasionally be so small that it would not surpass the threshold, e.g., when it is on the order of hundreds of particles on top of a low (e.g., < 100 cm^{-3}) natural concentration (baseline concentration).~~

310 ~~Generally, concentration data from remote regions, characterized by the absence of dominant local (anthropogenic) sources, vary only slowly with time, compared to when influenced by local pollution. This means that the concentration gradient (time derivative) is small. In contrast, concentration data show distinct variations, such as rapid fluctuations, when affected by pollution from nearby sources (e.g., Fig. A4). The PDA builds on this abrupt variation in concentration and detects polluted data based on the rate and magnitude of change in the concentration signal over a given time period. The basic principle of the~~

315 ~~PDA was developed and used for the 2018 Microbiology Ocean Cloud Coupling in the High Arctic (MOCCHA) campaign on the Swedish ice breaker *Oden* by Baccarini (2021). Here, we further develop this algorithm and test it against different datasets. Importantly, the algorithm is only based on target concentration data and does not rely on ancillary datasets, such as particle size distribution or meteorological variables. This brings the advantage that the PDA is applicable to a large number of datasets measured in remote environments (e.g., polar observatories, continental and marine background measurement sites~~

320 ~~or ship expeditions).~~

~~We also provide an open-source, python-based, tool for download on zenodo (https://doi.org/10.5281/zenodo.5761101), including a manual, which allows users to apply the same method to other datasets.~~ The PDA consists of a set of filters which can be applied in various combinations to identify polluted data. Figure 2 shows a schematic of the workflow. First, data points with a ~~gradient~~derivative exceeding a given threshold are tagged as polluted (Sect. 2.3.1). Second, a simple threshold filter

325 tags data points which exceed a specific threshold, e.g., > 10^4 cm^{-3} in our case because such concentrations are beyond the expected range for the central Arctic (see Sect 2.3.2). Optionally, for every tagged data point, the neighboring point can be tagged, too (Sect. 2.~~3~~4.3). An optional median filter identifies outliers in the dataset which are left untagged (Sect. 2.3.4). Lastly, sparse data points left untagged in a series of tagged data points are also tagged (Sect. 2.3.5). Individual parameters and thresholds in each step can be adjusted to customize the PDA and to adjust its strictness. The neighboring and the statistical

330 median filters are optional and can be skipped, for example if the resulting segregation of polluted data points satisfies the needs of the user already after the first steps. This allows retaining more data points in the final dataset. The different steps of the PDA are explained in detail in the following subsections. Table 1 summarizes all the parameters of the PDA described in Sect. 2.

11
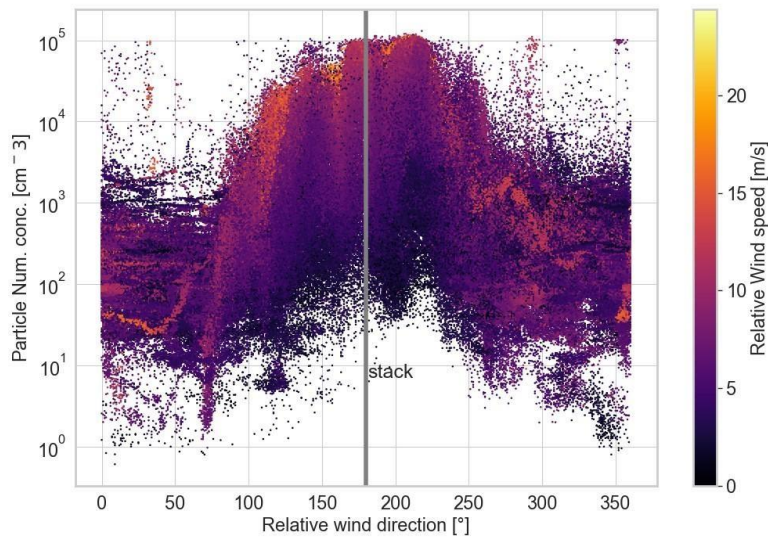
335

Figure 1: Particle number concentrations averaged over one minute as a function of relative wind direction (0° indicates wind coming from the bow) and color-coded by relative wind speed. Concentrations were higher with winds from the broader direction of the stack (located at 180° from the inlet position, this position is marked with a vertical line).

340
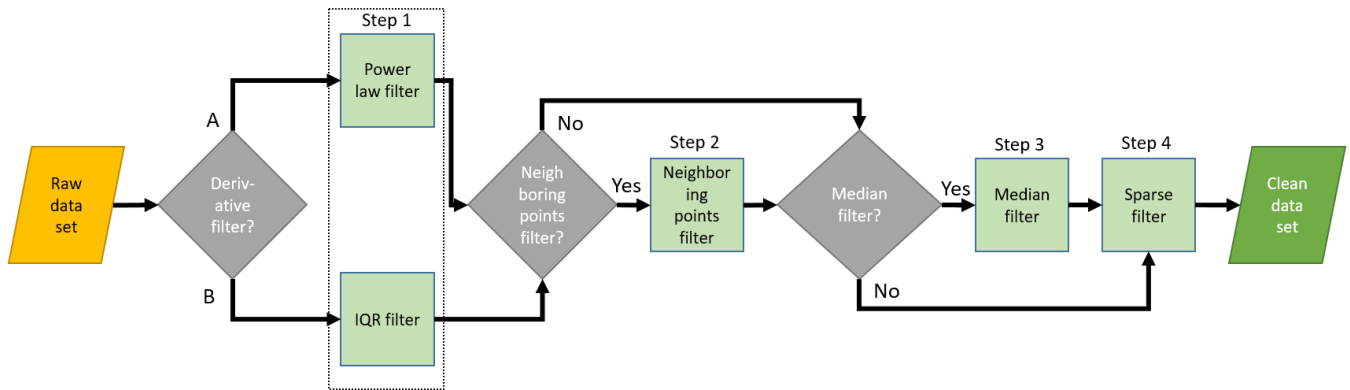
Figure 1: Schematic of the pollution detection algorithm. The key is the power law filter (highlighted in a dotted rectangle), which is followed by a series of steps. The neighboring points and the median filter are optional and can be skipped. Parameters of each step can be adjusted. IQR stands for interquartile range (see Sect. 2.4.1).

345

12

2.4.1 Step 1 and 2: ~~Gradient~~Derivative and threshold filter

The ~~gradient~~derivative filter is used to separate periods characterized by rapid fluctuations in concentrations (we consider them as polluted periods), from those dominated by slow changes in concentration (we consider them as unaffected periods). At

350   each data point in the native time resolution (10 s in our dataset) we calculate the absolute value of the time derivative (i.e., change in concentration~~the gradient over time~~) of the concentration using the central differences formula.

$$|dC'_t| \approx \left| \frac{C_{t+1} - C_{t-1}}{2} \right|$$ Eq. (1)

where dC'_t refers to the derivative of concentration C at time t. C_{t+1} and C_{t-1} refer to the previous and following measured

355   concentrations at time (t+1) and (t-1), respectively. Note that the derivative cannot be calculated with Eq. (1) at the edges of the dataset (very first and very last data points in the time series). Instead of the derivatives, the algorithm calculates the difference between the first (last) two data points at the beginning (end) of the dataset and uses those values for the derivative filter. This ensures that the edges of the dataset are also considered in the PDA. The derivative filter also ignores data gaps. For data points at the beginning and the end of a data gap, the derivative will still be calculated considering the previous and

360   following data points, regardless of the duration of the gap (see Eq. 1). ~~where $\left(\frac{dC}{dt} \right)_t$ refers to the time derivative of concentration C at time t, $C_{t+\Delta t}$ and $C_{t-\Delta t}$ refer to the concentration C at time $t + \Delta t$ and $t - \Delta t$, respectively. Δt refers to the time interval between two data points.~~ To separate polluted from unaffected data we developed two methods:

Method A separates polluted from unaffected data with a power law. We average the time derivatives of the particle number concentration over one minute (6 values) and plot them against the one minute-averaged particle number concentrations (Fig.

365   3). The averaging time can be varied and adapted to datasets with different time resolutions. This is discussed in Sect. 3.1. We choose one minute for a pragmatic reason: At one minute time resolution we can still see influences of short-lived changes in particle number concentration (e.g., from ~~pollution~~contamination) and it makes data processing faster as the size of the one-year long dataset is large. Figure 3a shows two "branches" of data points (visually emphasized by the relative wind direction color code): One with higher ~~gradients~~ derivatives representing periods of high concentration variability, i.e., due to local

370   ~~pollution~~contamination, and one with lower ~~gradients~~derivatives, indicating smooth variation, i.e., not affected by local ~~pollution~~contamination. Separating the polluted and unaffected branch is the fundamental step of the PDA developed here. The ~~time~~ derivative of the particle number concentration can be described as a power law of the particle number concentration, and the two branches distribute around two different power laws. Thus, for the separation, we use a power law ~~($y = a * x^m$)~~ between those two branches

375   $$(y = a * x^m) \qquad\qquad\qquad\qquad\qquad Eq.\ (2)$$

m corresponds to the slope, and $log(a)$ to the intercept with the logarithmic y-axis. Values for the power law fits are empirically selected.

13

(*m* corresponds to the slope, and $log(a)$ to the intercept with the logarithmic y-axis). Values for *m* and *a* have to be determined empirically to place the line between the two gradient branches. An approximate first value for *m* and *a* can be found by

380   extracting two points *(x1, y1)* and *(x2, y2)* from the graph:

$$m = \frac{\log(y_2/y_1)}{\log(x_2/x_1)} \qquad\qquad \text{Eq. (2)}$$

$$a = y_1/x_1^m$$

$$\text{Eq. (3)}$$

385   Finding optimal values for *a* and *m* is an empirical process which can be ~~verified~~ validated by looking at the time series of the polluted and unaffected data together. This process likely needs several iterations until values for *a* and *m* are found which satisfy the needs of the intended data analysis. A higher slope in the separation line means that, for a fixed particle number concentration, the threshold of separation moves towards higher ~~gradients~~ derivatives of particle number concentration, and therefore allows more variability in the data, i.e., the method is less strict. A higher intercept sets the threshold of separation

390   to higher ~~gradients~~ derivatives at lower concentrations, allowing for more variability there. Examples of four different separation lines are shown in Fig. 3a. For the MOSAiC dataset, we found a value of m = 0.55 s^{-1} and a = 0.5 cm^{-3}s^{-1} (red line) to work well with our dataset (see Sect. 3.1).

Method B separates data based on the interquartile range (IQR) of the ~~gradient~~derivatives within a defined period. Not all datasets show an equally clear separation of the ~~gradient~~derivatives into two branches like the particle number concentration

395   shown in Fig. 3a. An example is the particle number concentration dataset from Jungfraujoch (Fig. 3b). An alternative method is thus to separate polluted from unaffected data based on the deviation of the ~~gradient~~derivatives from their centered IQR. For this, we calculate the centered IQR of the ~~gradient~~derivatives of each data point in a moving ~~window of a set duration~~ time window (called IQR window) (24h in the case study described in Sect. 3.4.4, which is equal to 1440 data points). This means that for each data point, we calculate the IQR from the data +/- half of the IQR window before and after the data point. When

400   the absolute ~~gradient~~derivative of a data point exceeds the 75th percentile by a given factor (hereafter called IQR factor), the data point is flagged. We use an IQR factor of 1.7 to identify ~~pollution~~contamination in the JFJ dataset. Both the IQR window size and the ~~separation~~ IQR factor of the IQR method can be adjusted in the PDA code. Method B is well suited to separate datasets with less obvious difference between pollution and unaffected periods. As a first start, we therefore suggest to try an IQR window size of 1440*x, where x is the time resolution of the dataset. We found the factor 1440 to work for datasets with

405   1 minute time resolution, where it represents a time window of 24 hours.

Note that the moving centered IQR can only be calculated for data points with a distance of half of the IQR window from the edges in the dataset. To also account for the edges of the dataset, we fill the first (last) data points with the calculated IQR value of the first (last) calculated data point. This means that the IQR is assumed constant for half of the IQR time window at the edges. In our case (with an IQR window of 24 h), this affects the first and the last 12 h of the dataset.

410 Simultaneously with the derivative filter, we introduce an upper and lower concentration threshold (step 2), as described below, beyond which data are removed. ~~Given the simplicity of this step, it is subsumed under the derivative filter step.~~

~~2.4.2 Step 2: Threshold filter~~

For specific regions, like the central Arctic in our case, one can assume concentrations not to exceed a certain threshold as long as they are not influenced by local ~~pollution~~contamination sources. Based on the particle number concentration dataset
415 throughout the whole MOSAiC and MOCCHA observation periods, we argue that it is safe to assume that particle number concentrations above 10^4 cm^{-3} can be considered as influenced by local ~~pollution~~contamination with the detection limits of the instruments used for the two campaigns. Note that new particle formation events, which typically lead to the highest number concentrations second to ship activities during the expedition, do not exceed this threshold. See Fig. 3, where the branch of unaffected data below the separation line does not show any data points $> 10^4$ cm^{-3}. A similar principle is applied to a lower
420 limit, here 60 cm^{-3}. Below this threshold, we assume the dataset is not influenced by ~~pollution~~contamination. This threshold helps to maintain the ~~baseline~~background when a sudden concentration drop (e.g., from a precipitation event) would trigger the ~~gradient~~derivative filter. We choose 60 cm^{-3} to be a suitable threshold for this dataset because we did not observe such low values during polluted time periods, except in very rare occasions, but those data points would be detected by the sparse filter (sect. 2.3.5). Both thresholds can be adjusted in the tool, because they will vary with location, the detection limit of the
425 instrument, averaging time, and target compound. For example, a higher lower-limit threshold might be appropriate in a remote forest region, where lower particle number concentration limits can be as high as 500 cm^{-3} (Schmale et al., 2018). If the lower threshold is set to zero, all data below the upper limit threshold are included in the filtering algorithm. The threshold filter activates automatically with the application of the ~~gradient~~derivative filter. Hereafter we also mean the threshold filter when we talk about the ~~gradient~~derivative filter.

430

15
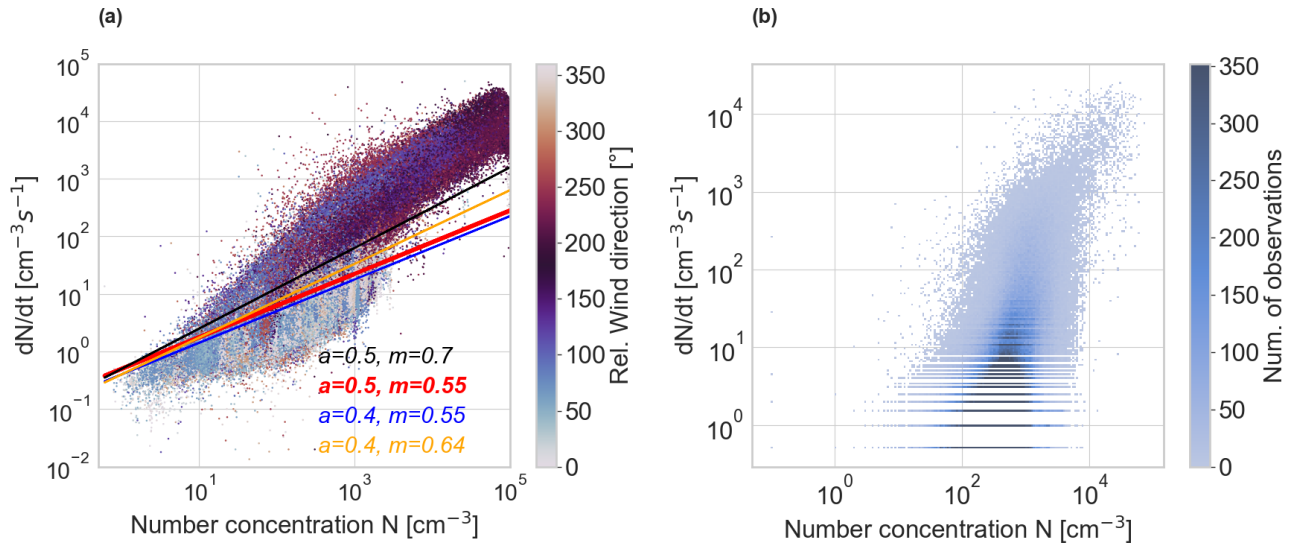
Figure 3: Absolute value of the minute-averaged particle number concentration ~~gradient~~derivative as a function of the minute-averaged particle number concentration. A) The dataset collected during the MOSAiC expedition. The color-code indicates the relative wind direction. The four lines show potential separation lines between polluted and unaffected data points for four different combinations of slope and intercept (y=a*xᵐ). Here we used the red line. B) The binned dataset collected at Jungfraujoch station in the Swiss Alps in 2016 (Bukowiecki et al., 2021). The color-code indicates the number of observations per bin.

2.4.2~~3~~ Step 3: Neighboring points filter

It can be useful to discard points at the beginning and end of polluted periods where single data points might not be tagged because the deviation of their values from previous or subsequent points is too small to be detected by the PDA. This filter targets data points at the transition from polluted to unaffected periods and vice-versa. Applying this filter is optional as it discards additional data, but in return results in a dataset less affected by local ~~pollution~~contamination. We show and discuss the results of this step in Sect. 3.1.

2.4.3~~4~~ Step 4: Median filter

The median filter aims at detecting false negatives, i.e. data points which are not representative of the background signal but were not flagged by the previous filter. For each data point, we calculate its deviation from the running median over a time interval (the median time interval). ~~Here, we define individual data points that exceed a defined factor above the running median as outliers. To detect such outliers, an additional filter, based on the running median of the concentration over a time interval (hereafter called median time interval), can be applied. For each data point, we calculate its deviation from the running median over the median time interval.~~ If the deviation exceeds a given factor above this median, it is flagged as ~~pollution~~polluted. The factor can be adjusted to lower (stricter) or higher (less strict) values with the trade-off of more false positive data points (i.e., unaffected data points flagged as polluted) or false negative data points (i.e., polluted data points

which are not flagged), respectively. We found an empirical deviation factor of 1.4 to support the detection of outliers for MOSAiC and keep the number of false positively detected data points as small as possible. This is further discussed in Sect. 3.1.

455

2.4.~~4~~5 Step 5: Sparse data filter

As a last step, we apply a sparse data filter to tag leftover unaffected data points in periods affected by local ~~pollution~~contamination. More quantitatively, if the ~~sum~~ number of polluted data points in a given time window (subsequently called sparse window) exceeds a given threshold (termed sparse threshold), all points in the sparse window are flagged as 460 polluted. We use a sparse threshold of 24 within 30 data points (which corresponds to 30 minutes in our case). The sparse threshold and the associated time-window can be adjusted in the PDA. The sparse data filter is automatically activated as the final filtering step. To de-activate the sparse data filter, one can simply set the sparse threshold to the same number of data points as in the sparse window.

465 **Table 1: Overview of all filter steps and parameters of the PDA applied to different datasets.**

Filter step	Parameter	Particle number concentration MOSAiC	Particle size distribution MOSAiC	CO_2 MOSAiC dataset	Particle number concentration JFJ	Particle number concentration CPCf
1A. ~~Gradient~~**Derivative** **filter (Power law)**	a m	$0.5\ cm^{-3}s^{-1}$ $0.55\ s^{-1}$	$1.4\ cm^{-3}s^{-1}$ $0.5\ s^{-1}$	- -	- -	$0.5\ cm^{-3}s^{-1}$ $0.5\ s^{-1}$
1B. ~~Gradient~~**Derivative** **filter (IQR)**	IQR factor IQR window size	- -	- -	1.5 24 h	1.7 24 h	- -
2. Threshold filter	Upper threshold Lower threshold	$10^4\ cm^{-3}$ $60\ cm^{-3}$	$10^4\ cm^{-3}$ $60\ cm^{-3}$	none none	$10^4\ cm^{-3}$ $60\ cm^{-3}$	$10^4\ cm^{-3}$ $60\ cm^{-3}$
3. Neighboring points filter	On/off	On	On	On	On	On
4. Median filter	Median time interval	30 min 1.4	30 min 1.4	30 min 1.001	30 min 1.5	30 min 1.3

	Median deviation factor					
5. Sparse data filter (no. of data points)	Sparse window Sparse threshold	30 24	10 3	30 20	30 24	30 23

3 Results and discussion

In this section, we present and discuss the performance of the PDA and compare the results to other commonly used approaches to identify local ~~pollution~~contamination (wind direction and visual inspection methods). We test the PDA on different types
470   of atmospheric measurements as well as on particle number concentration datasets with different time resolutions.

3.1 Performance of the PDA

First, we demonstrate the effect of the successive application of the various pollution filter steps, and second, we evaluate the performance of the final PDA settings against characteristic situations from the MOSAiC expedition. While the algorithm was applied to the entire dataset, below we show 24-hour case studies to illustrate the results.

475   Figure 4a-c shows, for the case study from March 6, 2020, how the individual filtering steps (the ~~gradient~~derivative filter, the ~~gradient~~derivative filter combined with the neighboring points filter and all filters together) affect the final cleaned particle number concentration dataset. The original time series is marked in red, while the cleaned dataset appears in blue. The case study shows a stable signal with concentrations around $100 \, cm^{-3}$, which is interrupted by a pollution event with particle number concentrations up to $10^5 \, cm^{-3}$ from 09:00 to 12:00 UTC. The ~~gradient~~derivative filter (Fig. 4a) detects the majority of the
480   polluted data points. Only 10 data points in this period remain untagged. Including the neighboring points filter (Fig. 4b) and the median and sparse data filters (Fig. 4c), removes all those points, improving the performance of the algorithm. Figure 4d shows histograms of the entire MOSAiC particle number concentration record for the original dataset, and after application of the ~~gradient~~derivative filter, the ~~gradient~~derivative and neighboring points filter and all filters. Concentrations below $200 \, cm^{-3}$ remain nearly untouched by all filters in the PDA. The strongest filter effect is visible at larger number concentrations (>
485   $3000 \, cm^{-3}$), where only a few counts remain in the cleaned dataset. In accordance with the threshold filter, number concentrations above $10^4 \, cm^{-3}$ are removed. The application of all the filters combined is not always necessary, as shown in Fig. A6. Here, the ~~gradient~~derivative filter already detects all the polluted data points and no further filters are needed. ~~This allows retaining more data for further analysis than when all filters are applied.~~ Table 2 shows how the year-round dataset is reduced in size after applying the ~~gradient~~derivative filter, the ~~gradient~~derivative and neighboring points filters, or all filters

18

490 combined. The second row shows the percentage of the original dataset that is left after applying the respective filters. After application of the ~~gradient~~derivative (and threshold) filter, 44 % of the data points are retained, showing the importance of the application of a filtering method in general. Applying further filtering with the neighboring points and median filters removes only 5 % and 1 % of additional data points, respectively. This demonstrates that the ~~gradient~~derivative filter alone captures the majority of locally polluted data points (90 %), while the additional filters have a "fine tuning" effect. This effect can still be

495 very important for individual cases as shown in Fig. 4a-c. Figure A7 summarizes the percentage of clean data per day after application of the PDA for the whole expedition. The data were most affected from ~~pollution~~contamination in spring and summer and least affected in winter. Note, this graph is indicative of ~~pollution~~contamination visible in the particle number concentration data and not necessarily for all atmospheric chemical and microphysical measurements taken during MOSAiC. To assess the effect of each filtering step, we applied each of them individually to the CPC3025 dataset and discuss this in

500 Appendix B.
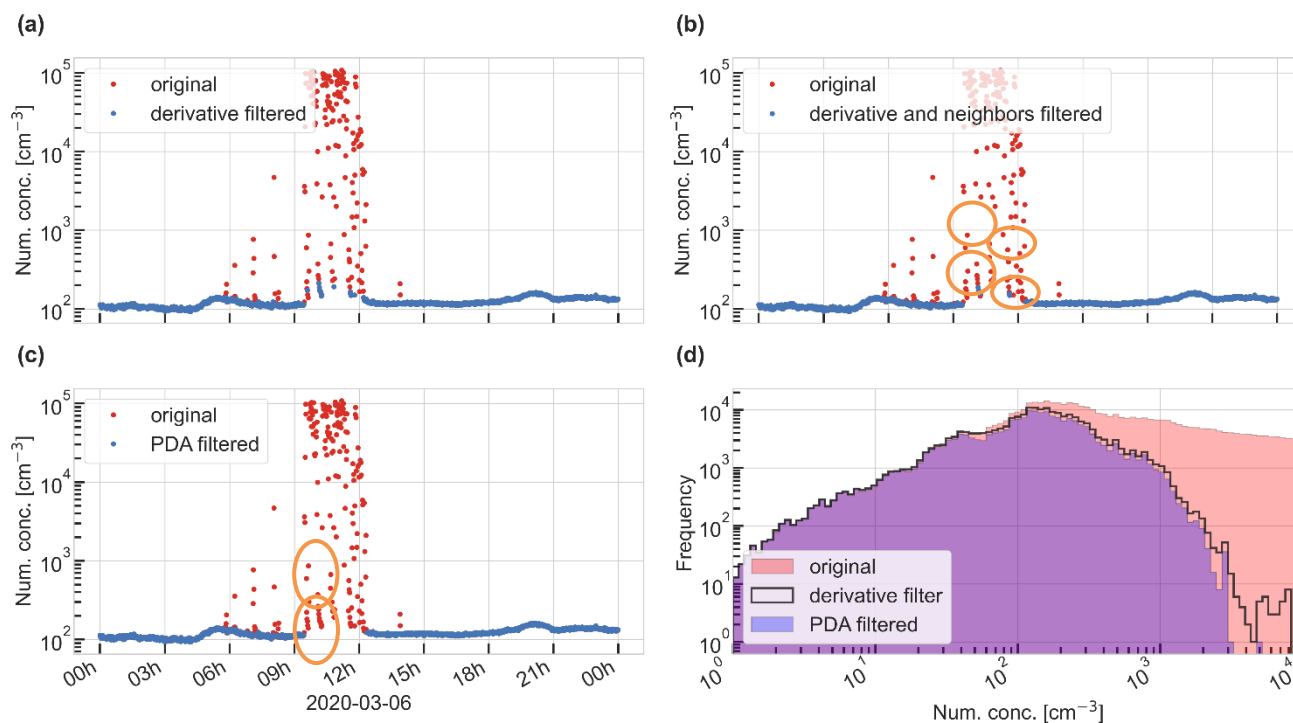
Figure 4: Comparison of the ~~gradient~~derivative filtering method with additional filtering steps. Cleaned data (in blue) are plotted over raw data (in red). a: only ~~gradient~~ derivative filter applied. b: ~~gradient~~ derivative and neighboring points filters applied. c: all

19

filters applied. d: Histogram of the ~~original (in red) and the~~ remaining datasets after steps ~~b~~a) (black contour line) and c) (purple). **"PDA filtered" means all options of the PDA were applied. For all plots we used data from the CPC3025. Raw data have only been** **pre-cleaned for zero filter measurements. The orange circles indicate areas where the additional filters remove additional data points.**

Table 2: Number of data points and percentage (relative to raw data) of data left when different filtering steps are applied. ~~The wind filter results are shown for comparison.~~

	Original data, no filter	~~Gradient~~Derivative filter	~~Gradient~~Derivative and neighboring points filter	All filters applied
Dataset size	521593	231269	204077	196628
Percentage	100	44	39	38

3.1.1 Case studies

Particle number concentrations in the Arctic can vary by orders of magnitude. To verify that the algorithm can be used in different environmental and ~~pollution~~contamination conditions, we tested its performance in characteristic situations throughout the expedition.

First, in conditions when the dataset is not affected by strong pollution spikes, it is required that the algorithm still detects small influences from local ~~pollution~~contamination. Figure 5a shows a day in January with a very stable and low boundary layer, resulting in a stable particle number concentration ~~baseline~~background around 150 cm^{-3} and occasional pollution spikes around noon. The algorithm successfully detects polluted data points and leaves the ~~baseline~~background untouched. In contrast, the wind filter would not detect any of the ~~pollution~~contamination. In this case, a stricter wind filter would not be possible since it would basically have to be extended to all wind directions. Second, under very polluted conditions, the requirement for the algorithm is to detect the full ~~pollution~~ contaminated period and to not leave polluted data points undetected (false negatives).

In Fig. 5b, a transition from unaffected to polluted conditions can be seen around 09:00 UTC due to changes in wind direction that resulted in stack exhaust contamination. The variability in the signal increases strongly and so does the gradient between data points. The PDA detects all relevant points as pollution. The wind filter would, in this case, also detect all the relevant points, but would become effective much earlier and thus detect false positives.

Third, new particle formation (NPF) and subsequent growth of particles is a common process in the Arctic which leads to an increase in particle number concentrations over a relatively short time (Kulmala et al., 2014; Baccarini et al., 2020; Schmale and Baccarini, 2021; Beck et al., 2021). This could potentially cause the ~~gradient~~derivative algorithm to accidentally flag

naturally high concentrations as pollution (false positives). We analyze one NPF event observed on June 21, 2020 where the particle number concentration increased from < 100 cm^{-3} to more than 1000 cm^{-3} within 3 hours (Fig. 5c). In addition, a few pollution spikes were observed during the NPF event. The ~~gradient~~derivative filter detects the pollution spikes and leaves the ~~baseline~~background untouched during the NPF-driven rise as well as during the subsequent drop in particle number

540 concentration later in the day. If a specific case study on this NPF event was done, the user could decide to apply the PDA only to this event and tune the parameters specifically. Here we show that the settings chosen for the entire campaign treat the NPF event adequately.

Fourth, another potentially challenging situation for the algorithm are wet-removal events. Aerosols can be washed-out of the atmosphere by rain or snow and their number concentration can decrease fast, leading to elevated ~~gradient~~derivatives. We

545 report such event observed on September 13, 2020 from 09:00 to 12:00 (Fig. 5d). The rate of change of the particle number concentration is not strong enough to cause false positives. These results demonstrate that the algorithm is able to deal with relevant situations and is therefore an adequate tool to clean particle number concentration datasets, which are influenced by both natural variability and local ~~pollution~~contamination sources.

To verify that the spikes in particle number concentration ~~can be assumed to be~~are caused by pollution and not by a natural

550 local (or regional) event, we compare the particle number concentration data during a pollution event with several other signals like nitric oxide (NO), CO and BC (Fig. A4). The main pollution spike in this example (ca. 18:00) coincides with the NO signal, which also shows a distinct spike at the same time (panel a). The BC signal also reacts during this event with elevated concentrations (panel d). The CO signal does not react at this time. Note, that the CO signal does not react strongly to ship pollution. This is in agreement with what we observed during the expedition and highlights the issues in operating the

555 automated purge system in the AOS container (Sect. 2.1). The ship exhaust from RV *Polarstern* during the MOSAiC expedition did not consistently show elevated CO signals that could allow CO to be used to identify pollution reliably. However, there were cases where apparent pollution events did result in higher observed CO concentrations. During the event described here, there are two minor spikes at 08:00 and 10:00 where the particle number concentration shows spikes that coincide with the CO signal (panel b). In contrast to the first example at 18:00, the wind direction was not coming from the

560 stack. This points towards a different local source of ~~pollution~~contamination, e.g., a skidoo, snow groomer or ship vent. These indicators let us conclude that the particle number concentration signal is sensitive to ~~pollution~~contamination from different sources and therefore provides a good base for the development of the PDA.
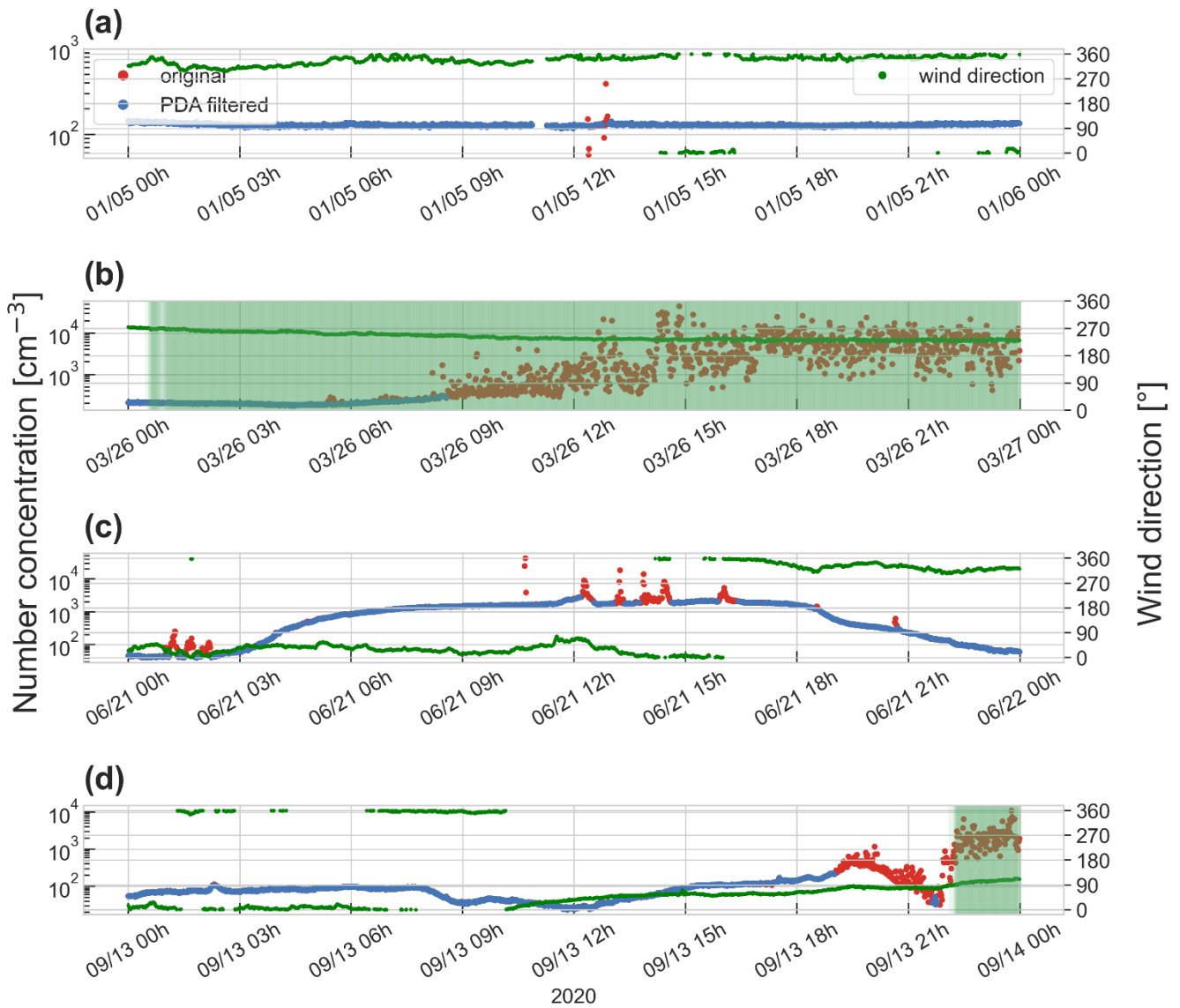
Figure 5: Performance test of the PDA method in four different situations. a) Under overall stable conditions, b) Transition from clean to polluted conditions, c) A natural increase in particle number concentration due to new particle formation, and d) A natural decrease in particle number concentration due to a precipitation event (freezing rain) in the morning (from 9 to 12 UTC). Green shaded areas indicate where the wind filter would flag data as polluted. Green points show the wind direction, red points show the raw particle number concentration, overlaid with the cleaned data points in blue.

3.1.2 Application of the PDA to particle size distribution

We applied the PDA with the parameters given in Table 1 to the measured total particle number concentration time series (i.e., the sum of the concentration of all size bins) of an SMPS dataset, collected during the MOSAiC expedition in the *Swiss*

22

575 *Container*. The result is shown in Fig. 6 on a seven days subset of the particle size distribution (PSD) dataset. The polluted periods are clearly visible in the PSD and show as distinct yellow vertical lines. At the same time, the total number concentration shows strong spikes. The PDA detects the polluted periods (shown as red data points) and leaves unaffected data (shown as black data points). This validates the functionality of the PDA. The SMPS data have a time resolution of three minutes, which shows the ability of the PDA to detect ~~pollution~~contamination in datasets with different time resolutions. More
580 tests of the PDA with datasets of different time resolutions are discussed in appendix ~~B~~C.
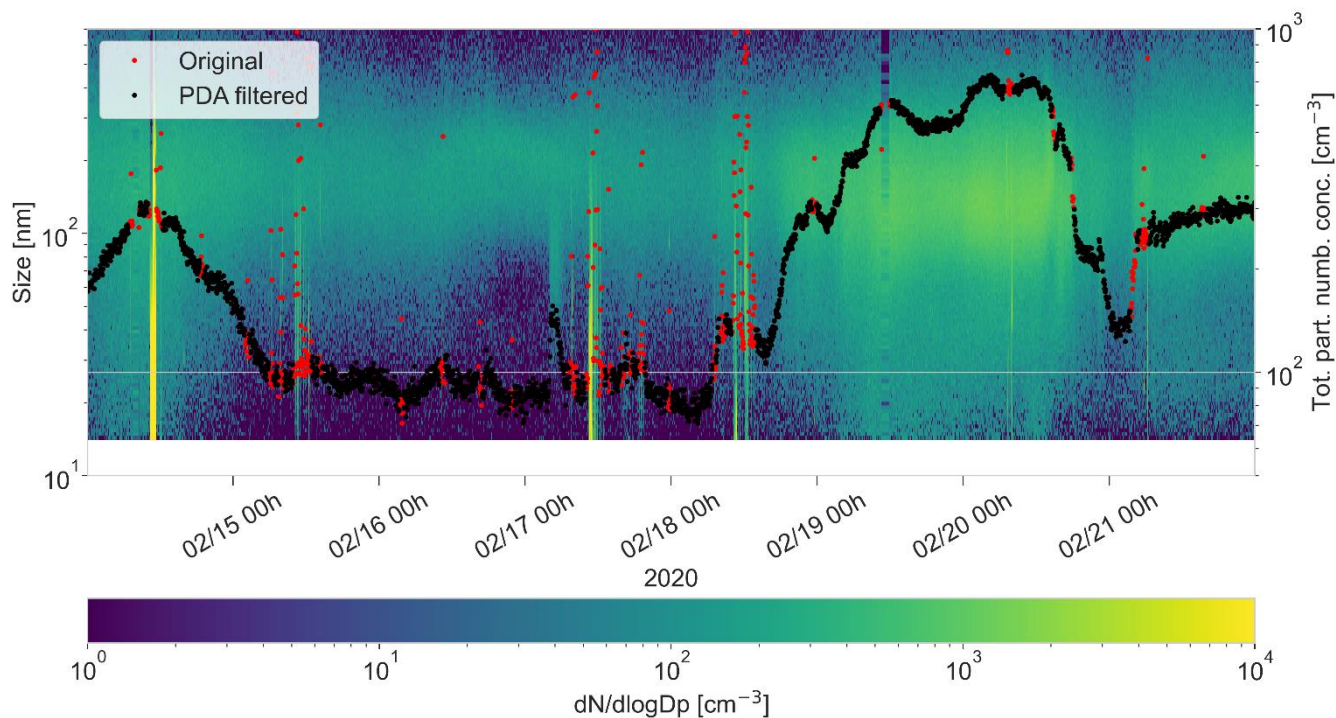
Figure 6: Application of the PDA to the total number concentration dataset (black line) collected by an SMPS. Data points identified as polluted by the PDA are marked in red. The dataset is plotted over the particle size distribution data of the same instrument.

585 **3.2 Comparison of the PDA to other commonly-used methods**

3.2.1 Comparison to the wind filter

The majority of pollution events is associated with wind arriving from the direction of the stack of the ship (Fig. 1). Thus, applying a simple filter based on wind direction might be sufficient to discard most polluted data. An example is shown in Fig. 7 where we assumed a polluted wind sector between $90°$ and $270°$ and marked all tagged data points with a red band. The
590 wind filter flags 59 % of the data as polluted, compared to the PDA, which flags 62%.. However, apart from detecting a large portion of polluted data, it also creates false positives, i.e., it flags unaffected data as polluted, as described in Sect. 3.1. It also does not detect any polluted data outside of the polluted wind sector. This is illustrated in Fig. 8 for the 17th of February, 2020,

23

where we compare the wind filter (panel b) with the PDA (panel a). On that day, the wind came from the port side of the ship and carried polluted air from a snow groomer. The PDA (panel a) detects and tags ~~all~~ more polluted data than the wind filter, ~~whereas the wind filter does not~~ (panel b). In addition, the PDA allows keeping unaffected data in the polluted wind sector (Fig.7). The wind direction method might, however, be simple and easy to clean data when the only source of local pollution is a point-source, and if the only ~~pollution~~contamination source is in a fixed wind direction from the measurement point. Although widely used on ship campaigns (see Sect. 1), the wind filter is not well suited for those campaigns, where multiple and moving emission sources exist.

600
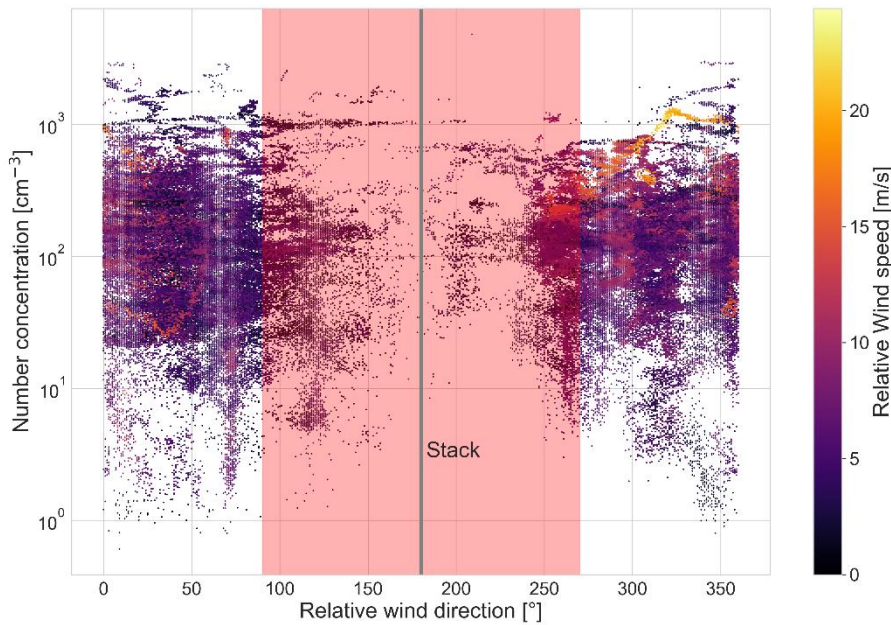
Figure 7: Same as Fig.1 but after applying the PDA to the dataset. Flagged data points were removed to visualize the data product after application of all filtering steps. The red shaded area indicates where the wind filter would flag polluted data (between 90° and 270° relative to the bow). The direction of the stack is marked at 180° as a vertical line.

24
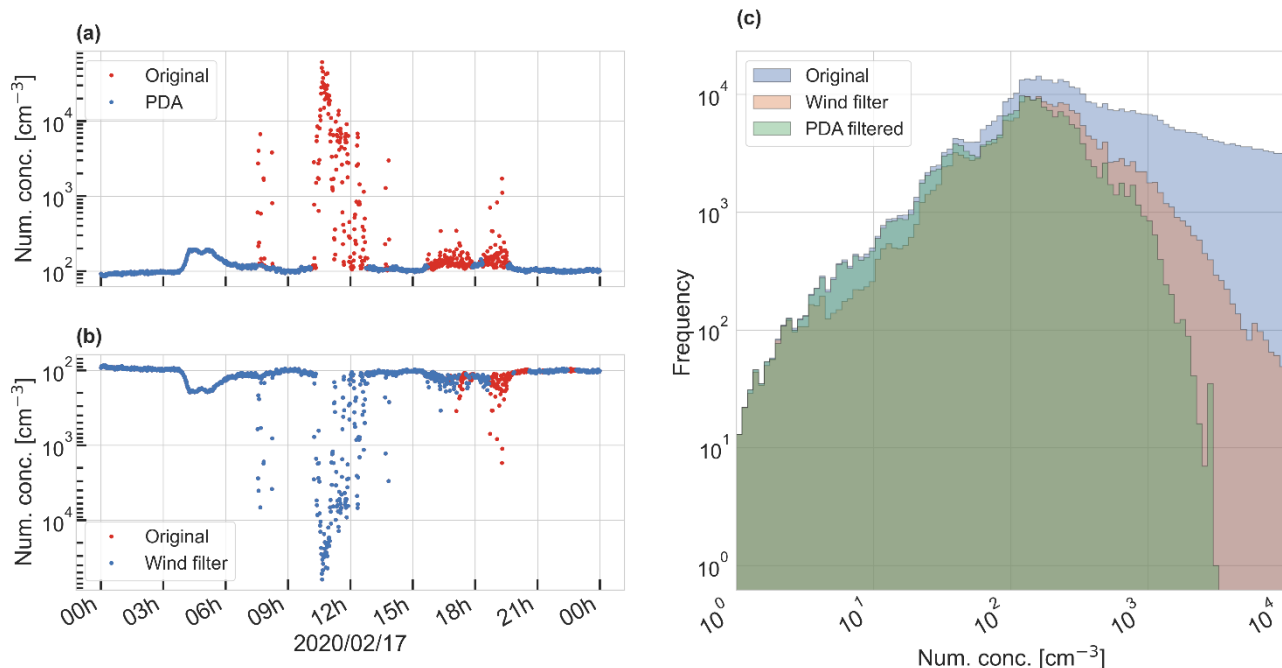
Figure 8: Comparison of the PDA (a) with the wind-based method, assuming a polluted-air sector of 90° to 270° from the bow (b, mirrored). Both filtered time series (blue) are underlaid with the original raw data (red). The wind-based filter method ~~is not case-sensitive and thus~~ cannot detect pollution events coming from other directions than the given wind sector. Panel (c) shows histograms of particle number concentrations before (blue) and after application of the PDA (green) and the wind mask (red).

3.2.2 Comparison of the PDA to the visual inspection method

We applied the PDA to a dataset independently cleaned by visual inspection and compared the results of these two methods. The dataset used for this test was collected from the ARM AOS container during the MOSAiC expedition. The visual filtering method is described in Sect. 2.3. The parameters used to apply the PDA to the dataset are listed in Tab. 1.

Both methods detect roughly the same fraction of clean data and agree in 93.9 % of all data points (see Table 3). The visual filtering method identifies slightly more clean data. Figure 9 shows the results of both methods in histograms. It shows the distribution of the raw data points (in grey) and the fraction of data points where the two methods do not agree, i.e., the fraction of data points which are identified as clean by the visual inspection but not by the PDA and vice versa.

The fact that the visual method keeps slightly more data points unaffected at lower concentrations compared to the PDA could be an indication that visual inspection detects slightly less false positives (unaffected data points detected as polluted). However, the advantage of the PDA is that it can be applied to other datasets with relatively little effort. Also, it applies strict thresholds to the dataset, which makes the result reproducible, while the visual filtering method depends on the users and their experience which makes it more prone to user bias. A comparison of both filtering methods in a time series is shown in Fig. A8.

Table 3: Fraction of clean data points of the derivative filtering method and the visual filtering method compared to the total number of data points (total counts) in numbers and in percent of the total counts. This table is based on the CPCf dataset in 1 min time resolution.

	# Data points	Percentage
Total counts	308750	100.00%
PDA clean	197671	64.02%
PDA polluted	111079	35.98%
Visual inspection clean	214540	69.49%
Visual inspection polluted	94210	30.51%
PDA clean, visual polluted	947	0.31%
PDA polluted, visual clean	17816	5.77%
Both clean	196724	63.72%
Both polluted	93263	30.21%

630 ~~Table 3: Fraction of clean data points of the gradient filtering method and the visual filtering method compared to the total number of data points (total counts) in numbers and in percent of the total counts.~~

	~~Total counts~~	~~PDA clean~~	~~Visual inspection clean~~	~~Both clean~~	~~Both polluted~~
~~Data points~~	~~308750~~	~~197696~~	~~214540~~	~~196719~~	~~93233~~
~~Percentage~~	~~100~~	~~64.0~~	~~69.5~~	~~63.7~~	~~30.2~~
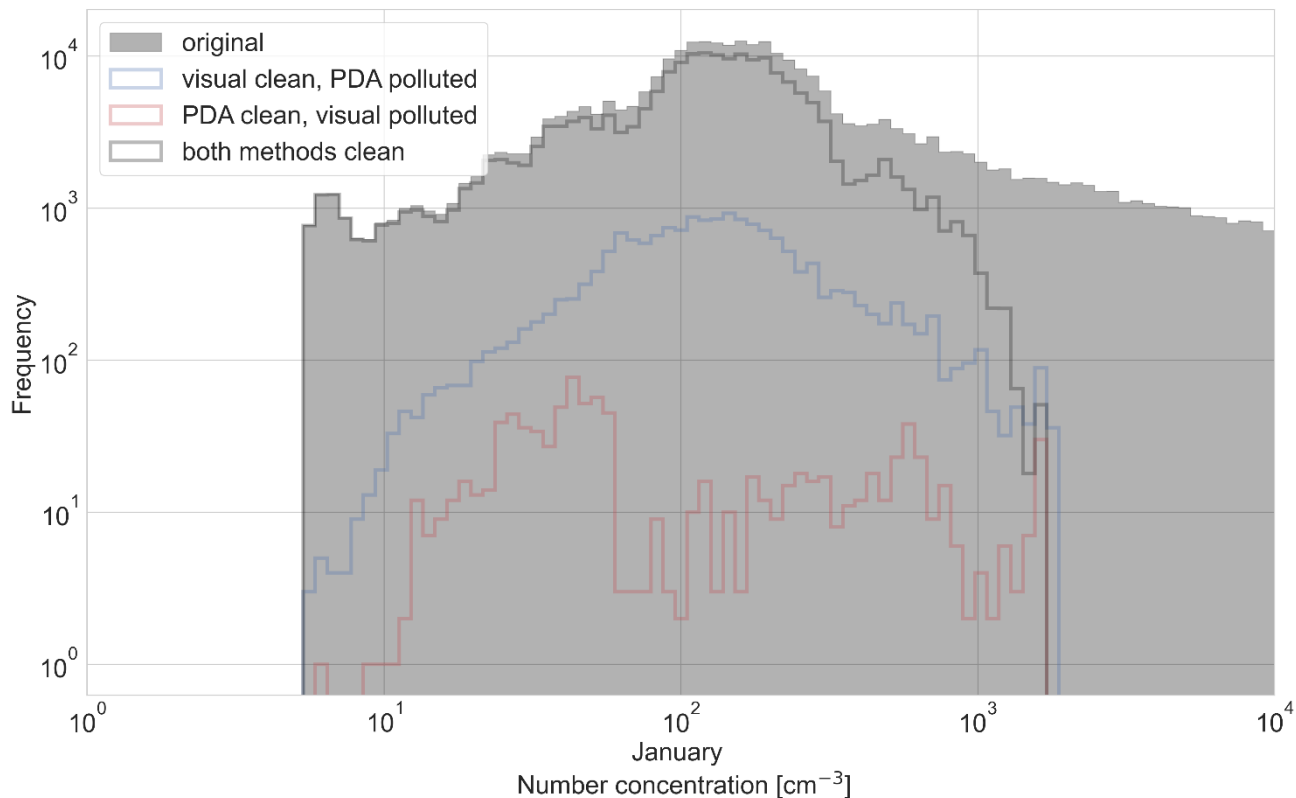
635

Figure 9: Comparison of the visual inspection method to the PDA on the dataset of the CPCf of ARM. Original data are shown in grey. The blue contour line shows the fraction of data points where only the visual inspection method, but not the PDA, considered data to be clean (6 %). The red contour line shows the opposite, i.e., the fraction of data points where only the PDA, but not the visual inspection method, considered data to be clean (<1 %). The dark grey contour line shows the fraction of data points where

640   both methods considered data to be clean (~64 %).

3.3 Broader application of the PDA

We test the performance of the PDA on datasets with different characteristics using time series of particle chemical composition and ambient air CO_2 concentrations collected during MOSAiC (see Sect. 3.4.1 and 3.4.2, respectively) and on a particle number concentration dataset collected at JFJ in the Swiss Alps (Sect. 3.4.3).

645   ### 3.3.1 Application to aerosol chemical composition datasets

To check whether the algorithm works on other datasets than particle number concentration data, we applied it to the ion fragment signal of $C_4H_9^+$ (m/z = 57) measured by the AMS, which characterizes fresh ~~pollution~~contamination from combustion. In a perfect scenario, our developed algorithm is able to group the signal of this fragment ($C_4H_9^+$) into high mass (and high ~~gradient~~derivative) resulting from ship emissions in comparison to low background mass concentration (and low

650   ~~gradient~~derivative), the latter associated with a relative wind direction away from the stack (90° to 270° relative to the bow).

27

Figure 10a shows the relation of the ~~gradient~~derivative of the mass concentration of $C_4H_9^+$ (averaged over 5 minutes) as a function of its mass concentration. We observe a separation of the ~~gradient~~derivatives into two branches with two different slopes as in Fig. 3a. However, the mass concentrations do not overlap in the two branches of the ~~gradient~~derivatives (dM/dt) of clean and polluted periods, therefore a separation based on the ~~gradient~~derivative is impossible. This is also visible based on the wind direction (indicated by the color); a separation between the 'pollution' and 'clean' data points occurs at approximately 10^{-2} µg/m^3, resulting in a critical concentration threshold rather than a defined slope. However, such a separation at a defined mass concentration grouped certain 'clean' data points into the 'polluted' category and thereby failed to produce a reliable pollution mask. Our hypothesis for the failure of the ~~gradient~~derivative algorithm when applied to AMS data is that the AMS has a lower particle cut-off of 70 nm and the > 70 nm particles detected by the AMS are affected by ~~pollution~~contamination in a different way than the entire particle population also containing smaller particles, as reflected by the CPC data, which contains particles as small as 3 nm. We found the typical peak diameter of ship pollution observed on RV *Polarstern* was approximately 30 nm. An alternative way to produce a pollution tag for AMS data is to apply a chemically resolved method, where the mass spectrum as a whole is compared to a previously defined chemical pollution spectrum. This method is described in more detail in Dada et al. (in prep.).

3.3.2 Application to trace gas datasets

Figure 10b shows the distribution of the ~~gradient~~derivatives for the CO_2 dataset. We used CO_2 data in a 1 s time resolution and averaged the ~~gradient~~derivative over 1 minute. The CO_2 signal varies by less than one order of magnitude when affected by pollution. The majority of the data points do not deviate from the observed atmospheric background concentration around 400 parts per million (ppm). The color-coded wind direction also gives no indication of separation of the data by wind direction. One reason is that the magnitude of the ~~gradient~~derivative of the CO_2 signal in case of pollution is low compared to its relatively high background concentration, and therefore, polluted data points do not separate clearly from the main "branch" of data points. Therefore, the separation of polluted and unaffected data points based on two branches of ~~gradient~~derivatives (step 1A) does not work for the CO_2 dataset. We thus applied the PDA with step 1B (the derivative filter based on the deviation from the running interquartile range) to the CO_2 dataset. ~~We thus applied the PDA with step 1B to the CO_2 dataset.~~ The parameters used for the PDA are shown in Table 1. An example of the resulting time series is shown in Fig. A9 on the same case study on July 27 as we described in Sect. 3.1.1. The CO_2 signal is noisy and shows a strong spike between 16:00 and 20:00. This spike matches the observations described in Fig. A4. The PDA detects and flags data points within the spike as polluted. Situations like this example with a noisy signal are further discussed in Sect. 3.5. Angot et. al. (in prep.) applied this method and describe the CO_2 dataset in more detail.
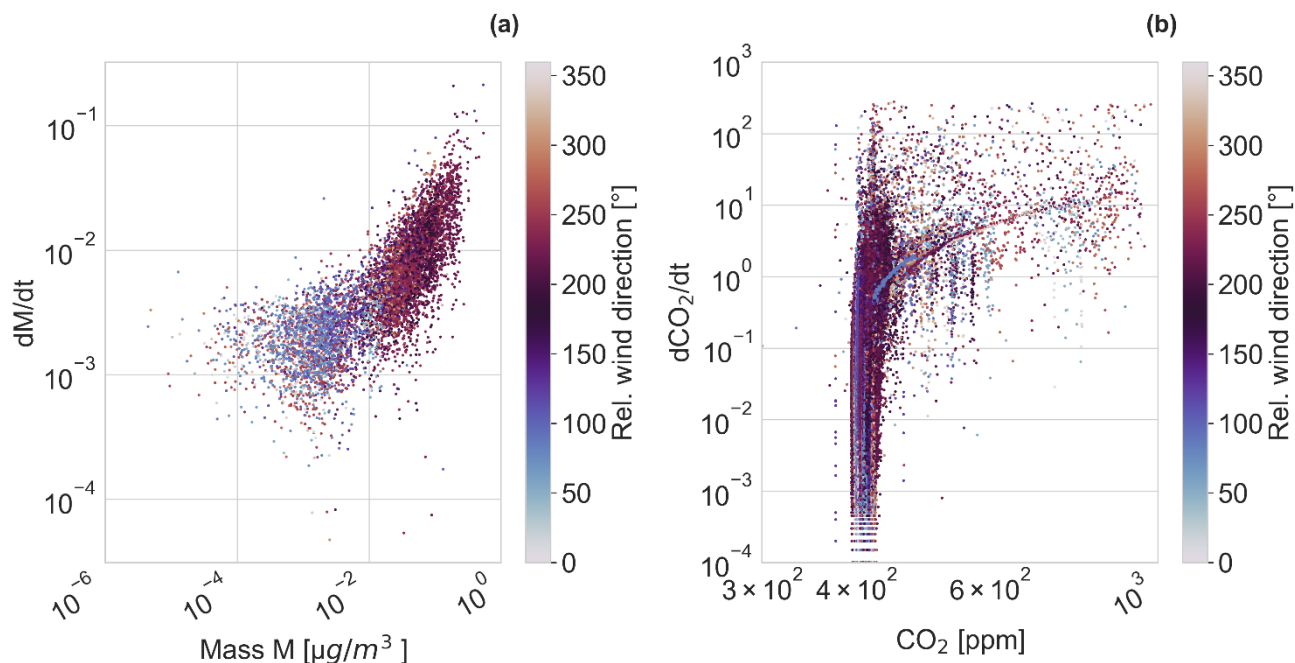
Figure 10: (a) ~~Time d~~Derivative of the ion mass signal of C_4H_9 (m/z=57) compared to its total mass concentration, measured by the Aerosol Mass Spectrometer. **(b)** ~~Time d~~Derivative of the CO_2 concentration signal compared to its concentration, measured by cavity ring-down spectroscopy. Colors indicate the relative wind direction.

3.3.3 Application of the PDA to a long-term high-altitude site monitoring dataset

We applied the PDA to a particle number concentration dataset collected at the high-altitude research station JFJ in the Swiss Alps. The data has a time resolution of 1 minute. The calculated ~~gradient~~derivatives show a very different pattern compared to those from the MOSAiC expedition (Fig. 3a,b). The difference in magnitude between ~~pollution~~contamination and the JFJ background dataset is much smaller (Fig. A10) compared to MOSAiC. The JFJ dataset is therefore well suited for separating polluted data using the IQR filtering method (step 1B). The parameters used in the PDA are shown in Table 1. The PDA was applied to an example time series from two days in July 2016 (Fig. A10), where a diurnal cycle of the ~~baseline~~background and pollution spikes during daytime are visible. This example demonstrates how the ~~baseline~~background is distinguished from the spikes even when the ~~baseline~~background varies by an order of magnitude. Given the different approach by Bukowiecki et al. (2021), i.e. detecting and counting spikes versus masking polluted time periods with the PDA, we cannot make a direct comparison between the two methods like in Sect. 3.2.2 (visual method). The final decision about flagging individual data points remains the user's responsibility and will depend on the objective of the analysis.

3.4 Limitations of the PDA

This study shows that the PDA is capable of cleaning ~~pollution~~contamination from a variety of particle and trace gas datasets.
700 However, a challenge for the algorithm remains to deal with false negatives, which are left after applying the ~~gradient~~derivative filter (step 1 of the PDA). In situations with small pollution peaks, which occur on top of a clean ~~baseline~~background, this is often the case at the beginning and at the end of the affected period. The application of the neighboring points filter on top of the ~~gradient~~derivative filter improves the result significantly, but might not catch all pollution-affected points. An example of this is shown in Fig. A11a and b.

705 Another challenge for the PDA is situations where the signal is influenced by subtle ~~pollution~~contamination, which does not result in large spikes but rather in a very noisy signal with low amplitude above a ~~baseline~~background. Two examples are shown in Fig. A9 and A11. These situations are also difficult to assess for an expert using the visual inspection method. The boundary between polluted and unaffected data is blurred, and the ~~gradient~~derivative filter in Fig. A11 only flags a subset of data points that protrude from the main signal. In this example, some of the flagged data points do not exceed the "baseline"
710 concentration at all. The difference between an unaffected and a flagged data point can be 2 cm^{-3} at concentrations of 190 cm^{-3}, or 10 cm-3 at 390 cm^{-3} (the derivative filter threshold depends on the concentration). If we choose a stricter derivative filter, for example, with a = 0.45 (instead of 0.5) and m = 0.5 (instead of 0.55), more data points are flagged as contaminated and hence less false negatives remain (Fig. A12).~~The application of a strict PDA with all filters included could avoid false negatives.~~ However, this might also remove unaffected data points, and it is up to the user to make this decision.
715 The applicability of the PDA to a dataset also depends on the response time of the instrument. A response time which is slower than the occurrence of pollution (i.e. the instrument cannot capture the sharp rise and fall in concentrations) leads to smaller ~~gradient~~derivatives of the measured particle number concentrations. This would set an upper limit to the measured ~~gradient~~derivative. Still, pollution could be detected as long as this upper limit is substantially higher than the ~~gradient~~derivatives of the natural signal. This does not matter for the measurements with the CPCs, since the response time is
720 typically lower than 1 second (Enroth et al., 2018). In essence, this issue is similar to recording data in coarse time resolution, which would smear out the difference in magnitude between ~~baseline~~ background and pollution (see Appendix ~~B~~C).

4. Conclusions

We developed a pollution detection algorithm (PDA) to identify periods of local ~~pollution~~contamination in atmospheric aerosol
725 and trace gas concentration time series. The PDA was successfully tested with particle number concentration datasets from two different sites - a ship-based expedition in the high Arctic Ocean and a background station in the Swiss alps affected by tourism - as well as with a CO_2 concentration dataset from the high Arctic. In comparison to the commonly used wind direction method to clean datasets, the PDA is capable of identifying ~~pollution~~contamination from different sources and directions and reduces false positive and false negative results. Compared to a visual filtering method the PDA identifies a similar amount of

730 ~~pollution~~contamination (41 % with the visual method compared to 43 % with the PDA). The PDA only uses the target concentration data and does not rely on ancillary datasets to identify polluted data points. It works for datasets with a relatively low ~~baseline~~ background where pollution spikes exceed the ~~baseline~~background significantly and the sampling rate is fast enough so that the ~~gradient~~derivative of polluted signals separates clearly from that of unaffected. "Fast enough" depends on the variability of the ~~baseline~~ background and occurrence of pollution. In our case the methods worked for time resolutions

735 between 10 seconds and 10 min. The PDA is primarily designed for remote locations, but it might also be applied to locations where local ~~pollution~~contamination interference is so frequent that the majority of data points exceeds the contribution from the underlying ~~baseline~~background in the period of interest, like in urban areas for example.

The relative magnitude of interference from local ~~pollution~~contamination varies between different measurement campaigns and may depend on the type of instrument. The PDA is best suited to identify primary pollution, i.e., for particle number

740 concentration, or trace gases directly emitted by the pollution source (e.g., CO_2), or size distribution datasets with a clear primary pollution mode. For other variables, such as for accumulation mode particle chemical composition data, which are not representative of the main pollution size range (around 30 nm), a different approach might be better (e.g., Dada et al., in prep.) because the PDA will discard too many data points.

The PDA is published open-source in a user-friendly code toolkit downloadable from zenodo

745 (https://doi.org/10.5281/zenodo.5761101). All PDA parameters can be adjusted to adapt it to specific datasets or to customize the filtering level for specific needs. This makes it flexible and allows its application to locations where no ancillary datasets might be available. It also allows a fast application to multiple datasets and provides an objective, reproducible method to identify local ~~pollution~~contamination in remote or background conditions.

750

Appendix A
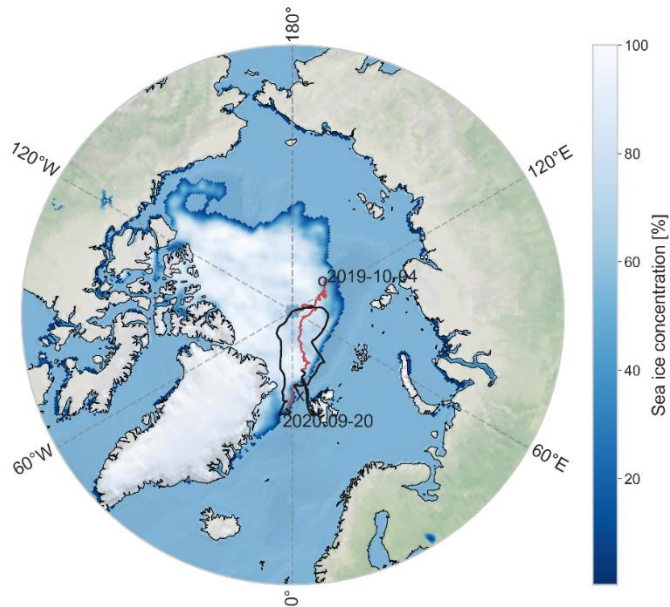
755 **Figure A1: Track of RV *Polarstern* during the MOSAiC expedition in the central Arctic (Schmithuesen, 2021a, c, d, e, b). Drift (red line) started in October 2019 and ended in September 2020. The black lines show periods where the ship was on transit. The sea ice extent is displayed from September 2019 at the annual minimum. We used sea ice data from the National Snow and Ice Data Center (Maslanik and Stroeve, 1999). The background map is made with Natural Earth (https://www.naturalearthdata.com/).**
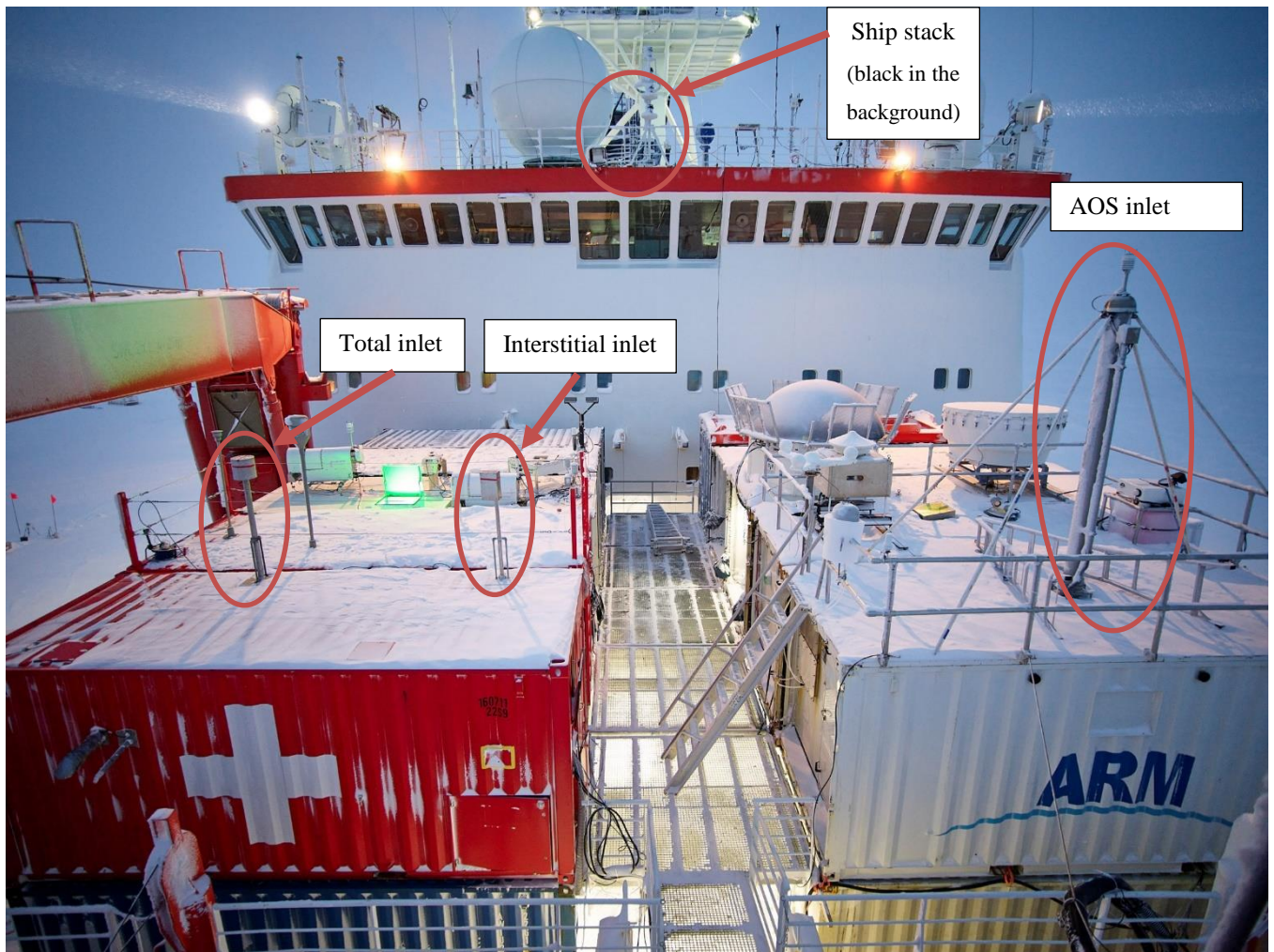
Figure A2: Bow of the ship during the expedition. In red with a white cross, the *Swiss Container* with its two inlets. The ARM measurements were performed on the port side of the ship in the white container at the front with a higher inlet. Photo credit: Michael Gutsche
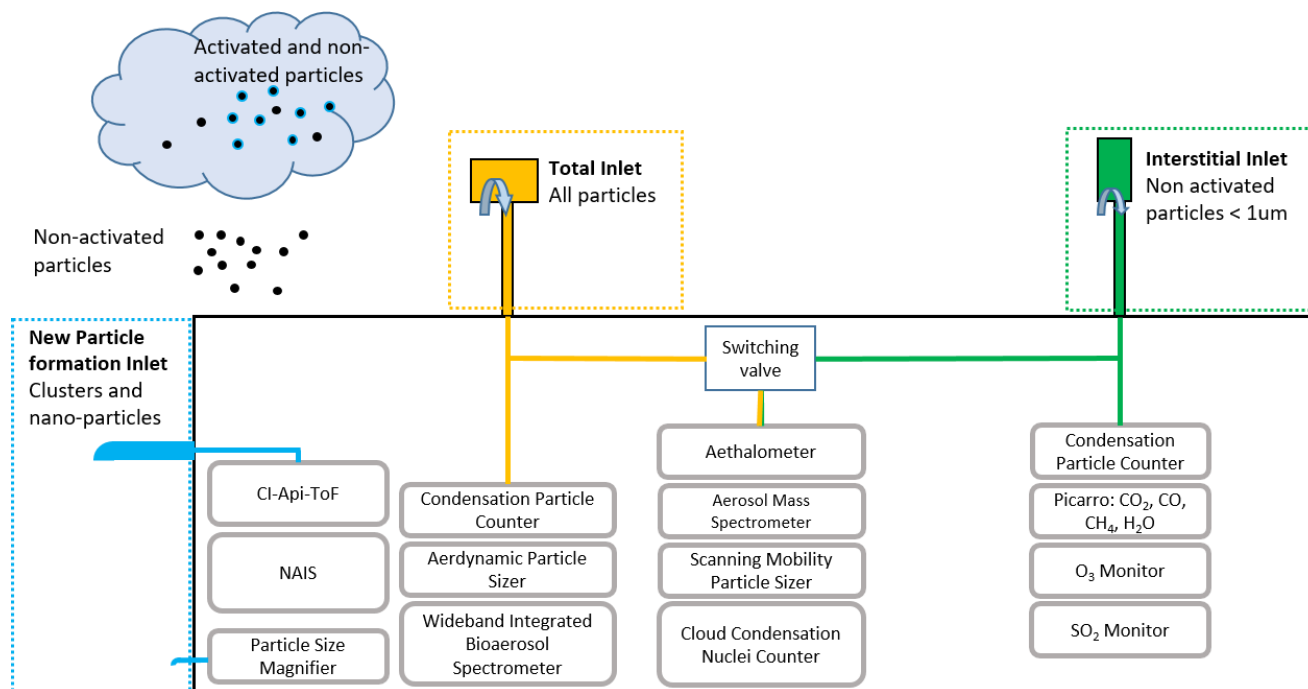
Figure A3: Full setup of the *Swiss Container* during the MOSAiC expedition (not all elements are discussed in this manuscript). In yellow the total inlet, in green the interstitial inlet. The valve switched between the two inlets to allow the instruments behind it (aethalometer, aerosol mass spectrometer, scanning mobility particle sizer, cloud condensation nuclei counter) to measure from both inlets. The blue inlet is the new particle formation inlet. CI-Api-ToF stands for chemical ionization atmospheric pressure interface time of flight mass spectrometer. NAIS stands for neutral cluster and air ion spectrometer.
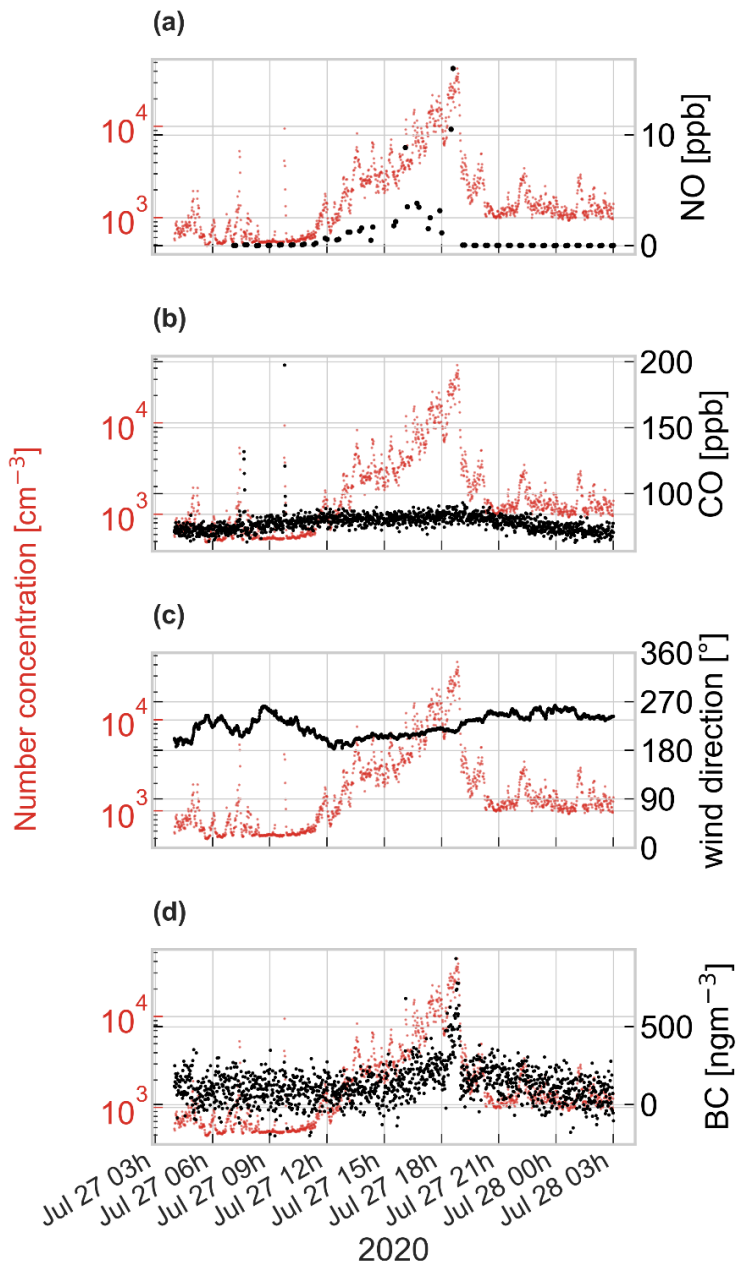
Figure A4: Particle number concentration (left axis) along with a) NO (in parts per billion (ppb)), b) CO (in parts per billion (ppb)), c) relative wind direction and d) equivalent BC (ng/m³) at 880nm with standard manufacturer settings for the correction factor and mass absorption cross section during a local ~~pollution~~contamination event in the afternoon of July 27, 2020. Starting around noon, the particle number concentration, NO and BC concentrations increased as wind came from the stack. Note that CO concentrations did not exhibit any significant variability during that event.

785
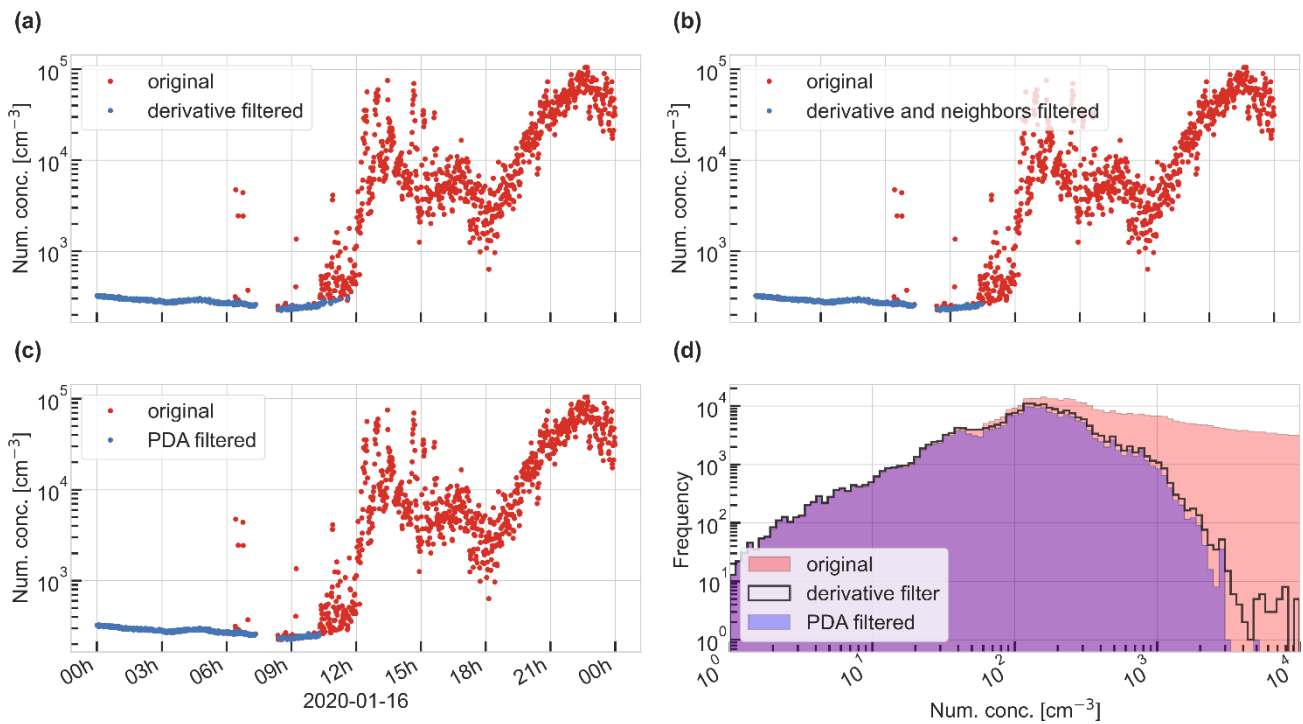
Figure A6: Same as Fig. 4 but for another day (January 16, 2020). Panels a-c show the original particle number concentrations data in red, overlaid with the unaffected data in blue. The application of additional filters in panels b and c do not show an effect. Panel d shows the distribution of the particle number concentrations of the complete dataset in ~~blue~~red, ~~and~~ after the application of ~~different~~ the gradient filter~~s~~ as a black contour line, and after the application of all filters of the PDA in purple. ~~in orange, green and red~~.
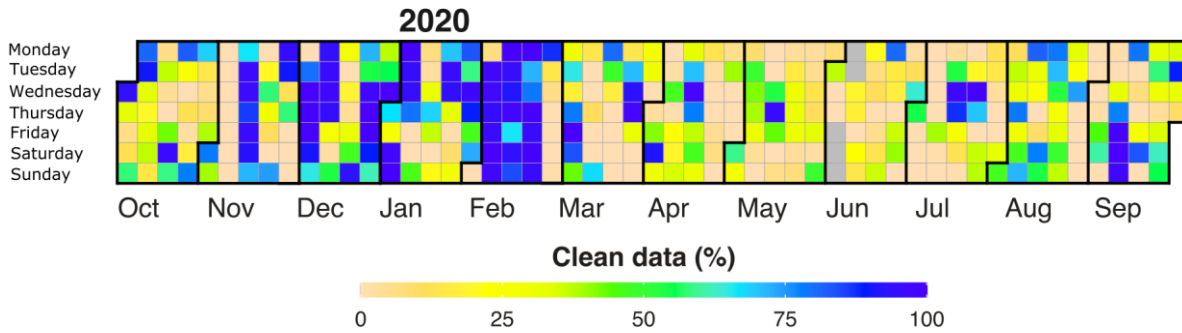
Figure A7: Percentage of clean particle number concentration data points per day during the MOSAiC expedition after application of the PDA. Missing data are indicated in grey and correspond to data removed when Polarstern was within Svalbard's 12 nautical miles zone. Please note this figure is indicative only and does not necessarily reflect the percentage of clean data points collected by other instruments during the expedition.
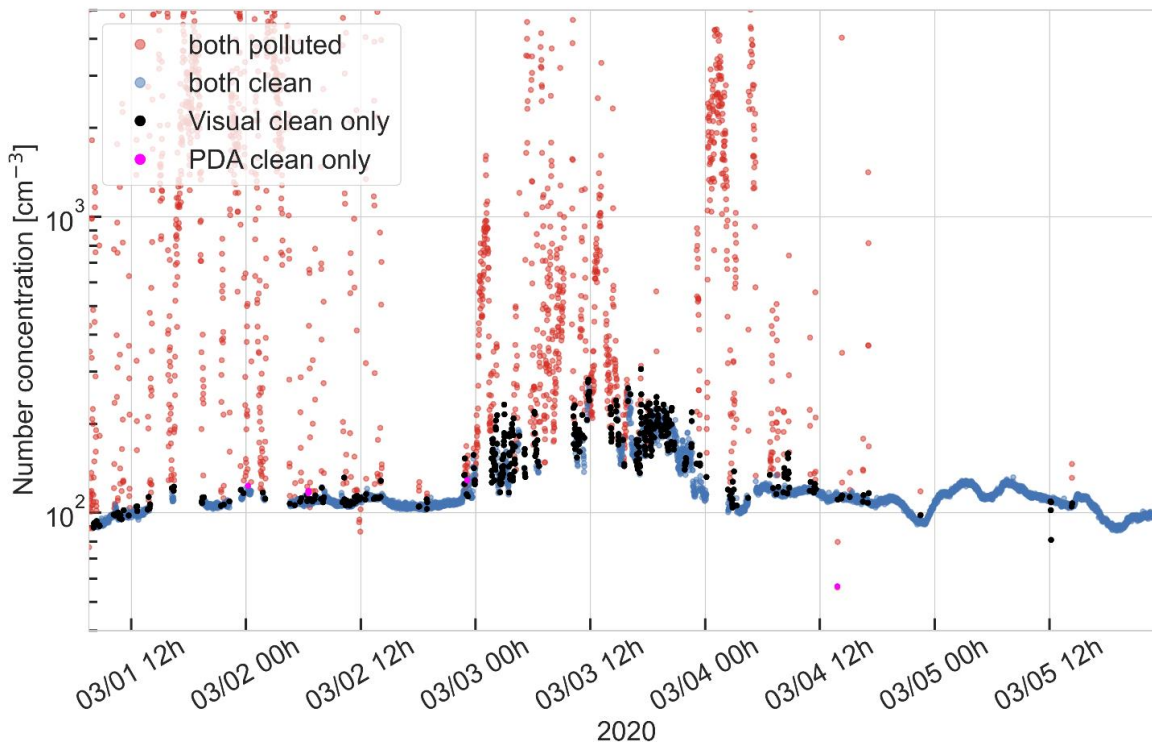
Figure A8: Time series with a comparison of the visual identification method and the PDA between 1 and 5 of March. In red: Data points which are detected as contaminated by both methods. In blue: Data points which are detected as unaffected from pollution

37

805
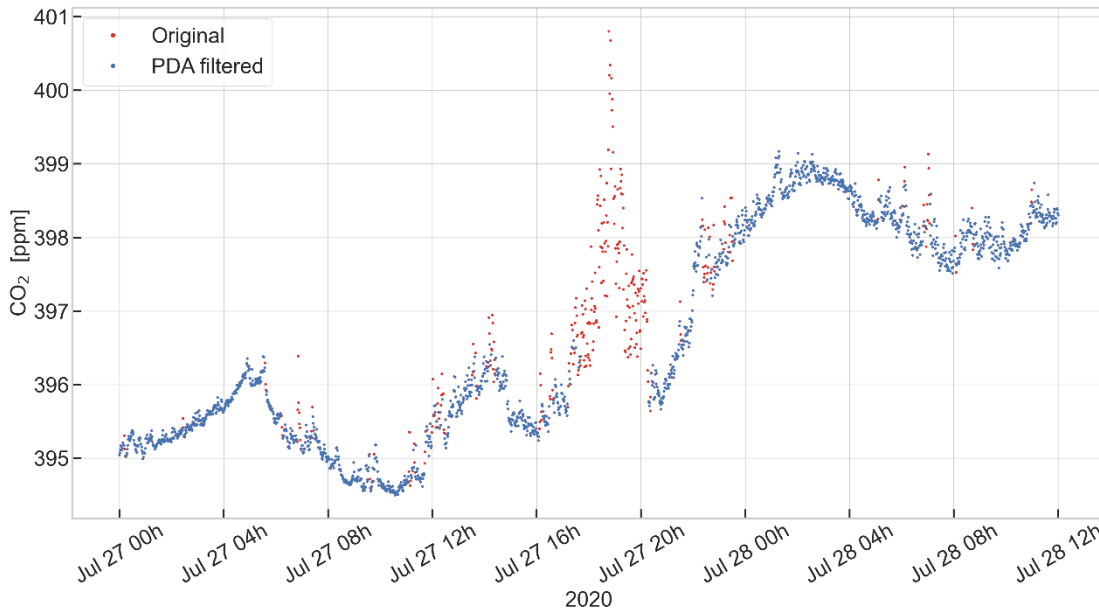
810

Figure A9. Time series of CO_2 mixing ratios after the application of the PDA using step 1B. Original data are shown in red, overlaid with unaffected data filtered by the PDA.

38
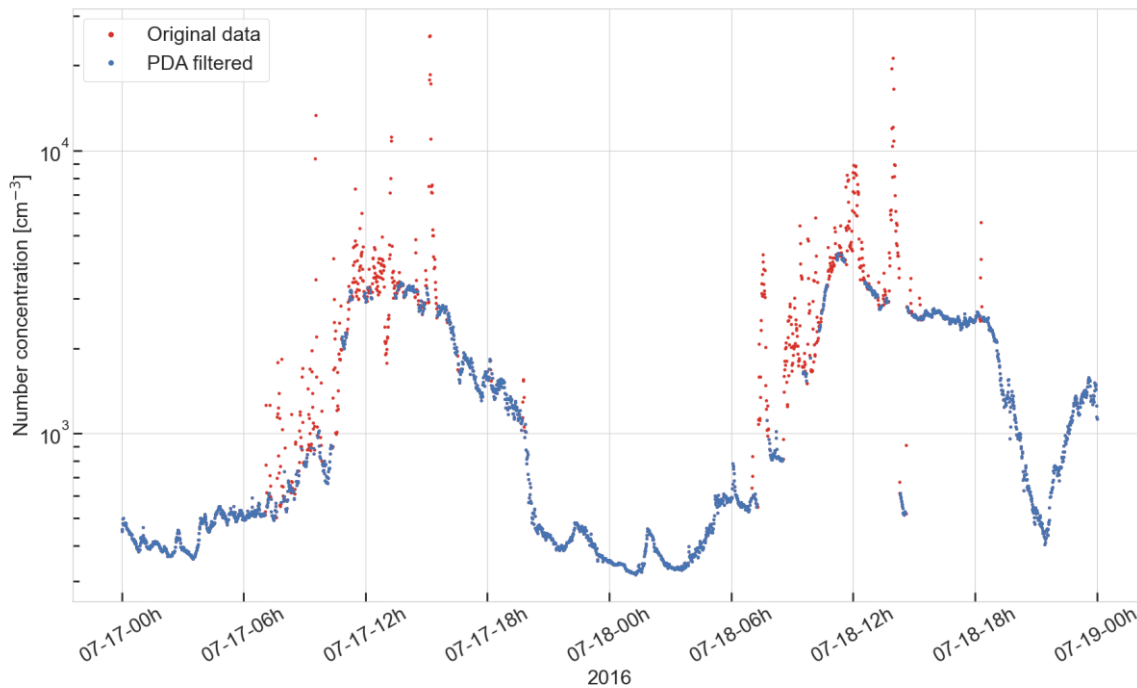
Figure A10. Time series of particle number concentration dataset from JFJ after the application of the PDA. Original data is shown in red, overlaid with unaffected data filtered by the PDA.

815
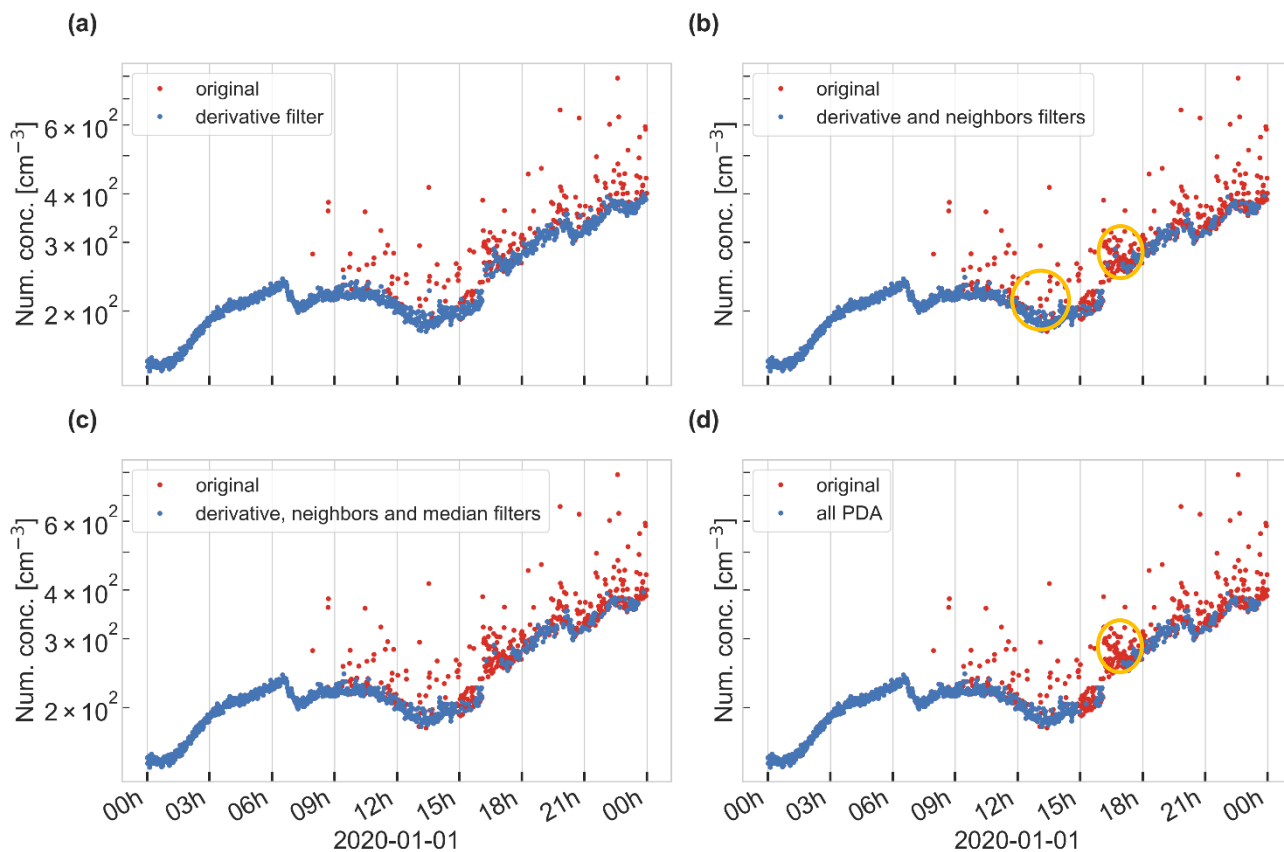
Figure A11: Case study of January 1, 2020. The particle number concentration signal is influenced by ~~pollution~~contamination which
shows as a noisy signal and not in distinct spikes. Panels a-d show the original particle number concentrations data in red, overlaid
with the unaffected data in blue after applying different filtering steps of the PDA. The orange circles highlight situations where
applications of the neighbors filter and the sparse data filter improve the detection of polluted data significantly.
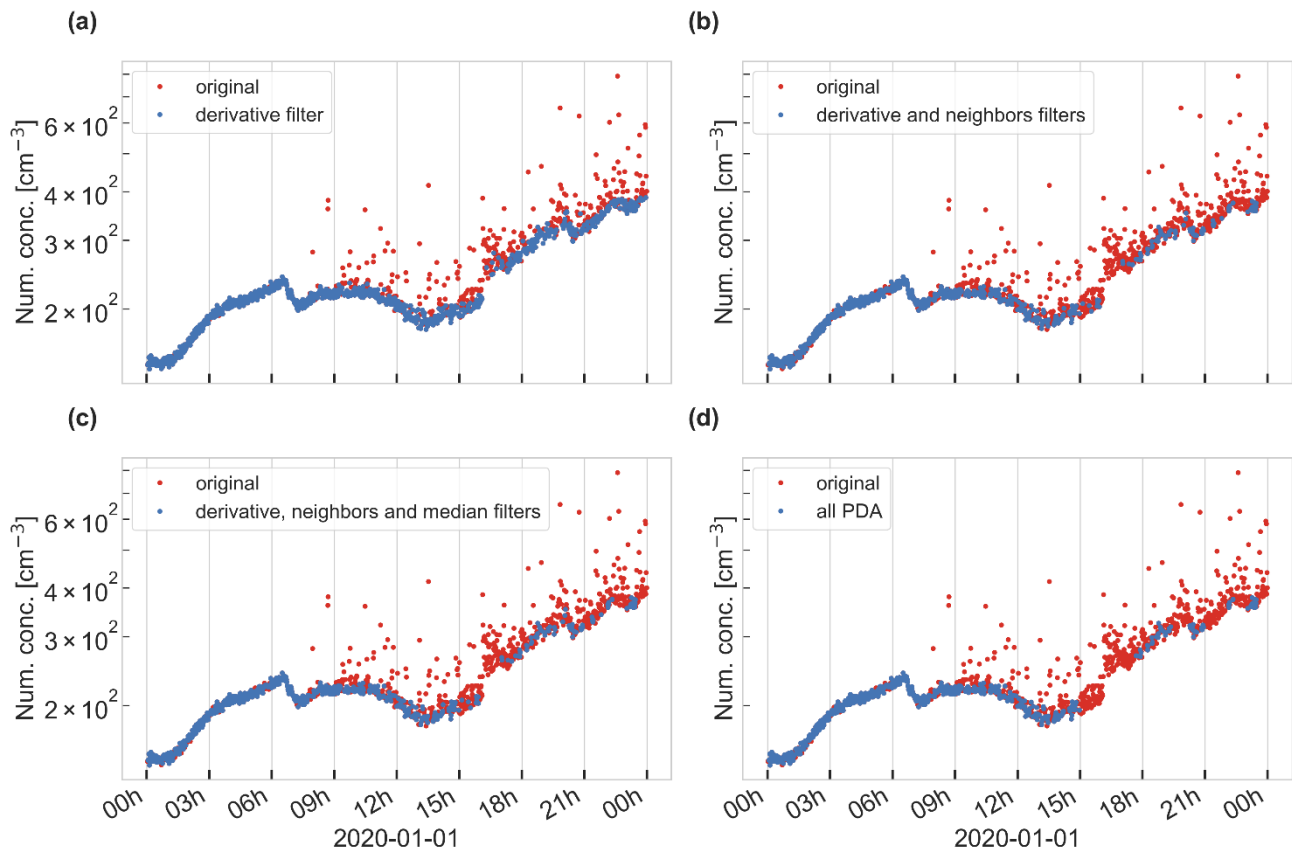
Figure A22: Same as figure A11, but with slightly stricter coefficients of the derivative filter. We chose a derivative filter with a = 0.45 and m = 0.5 to flag more data points in this case study.

Appendix B: Comparison of individual filtering steps

In figure B1, we compare how the application of each individual filtering step to the 1min resolution dataset of the CPC3025

830 performs on the case study from March 6th to March 8th. Panel a) shows the result after the application of the derivative filter and the lower threshold filter only (but not the upper threshold filter) with a = 0.5 and m = 0.55 and a lower threshold of 60 cm^{-3}. As we can see, the application of the derivative filter detects and flags most data points during the polluted time periods, but leaves some during the contamination event on the 6th of March. The application of the derivative filter leaves 43% of the data unaffected and it reduces the mean concentration from 5198 cm^{-3} to 202 cm^{-3}. Panel b) shows the application of the upper

835 threshold filter alone. Here we set the upper threshold to as low as 130 cm^{-3} to be able to retrieve the background signal as much as possible. With this threshold, 23% of the data are left unaffected with a mean concentration of 70 cm^{-3}. However, the application of a single threshold to a longer time series is difficult, since the background concentration can rise to higher concentrations (as can be seen for example in Fig. 6). The upper threshold can be useful in cases, when the measured concentration stays at the upper detection limit of the instrument over a long time period and thus the derivative filter would

840 not catch those contaminated data points. Panel c) shows the application of the median filter alone with a median window of 360 data points (6 hours) and a median threshold of 1.05. The application of the median filter alone with these parameters leaves 68% of the data unaffected, with a mean concentration of 2979 cm^{-3}. It is not satisfying because it is not able to flag the strong contamination on the 8th of March after 12:00. Too many contaminated data points raise the median concentration. The median filter relies on a pre-cleaned dataset, where most of the contaminated data points have been removed already. Therefore,

845 it can only be applied after the application of the derivative filter. Finally, Panel d) shows the result after the application of the whole PDA, with the parameters presented in Table 1. The application of the whole PDA leaves 38% of the data unaffected with a mean concentration of 191 cm^{-3}. Evaluated visually by expert's judgement, we find that it performs better than the application of the single filters, it detects more contaminated data points and results in a time series which represents the background concentration. Table B1 shows an overview of how many data remain unaffected after the application of the

850 different filtering steps. Additionally, the mean concentrations and the standard deviations are shown. The derivative filter is by far the most powerful step of the PDA, as it detects already 64% of the total contamination and reduces the mean concentration drastically. The other filters of the PDA only have a "fine-tuning" effect and add another 6% of flagged data points. This effect can still be very important for individual cases as shown in the case study during March 6 around noon (Fig. 4).
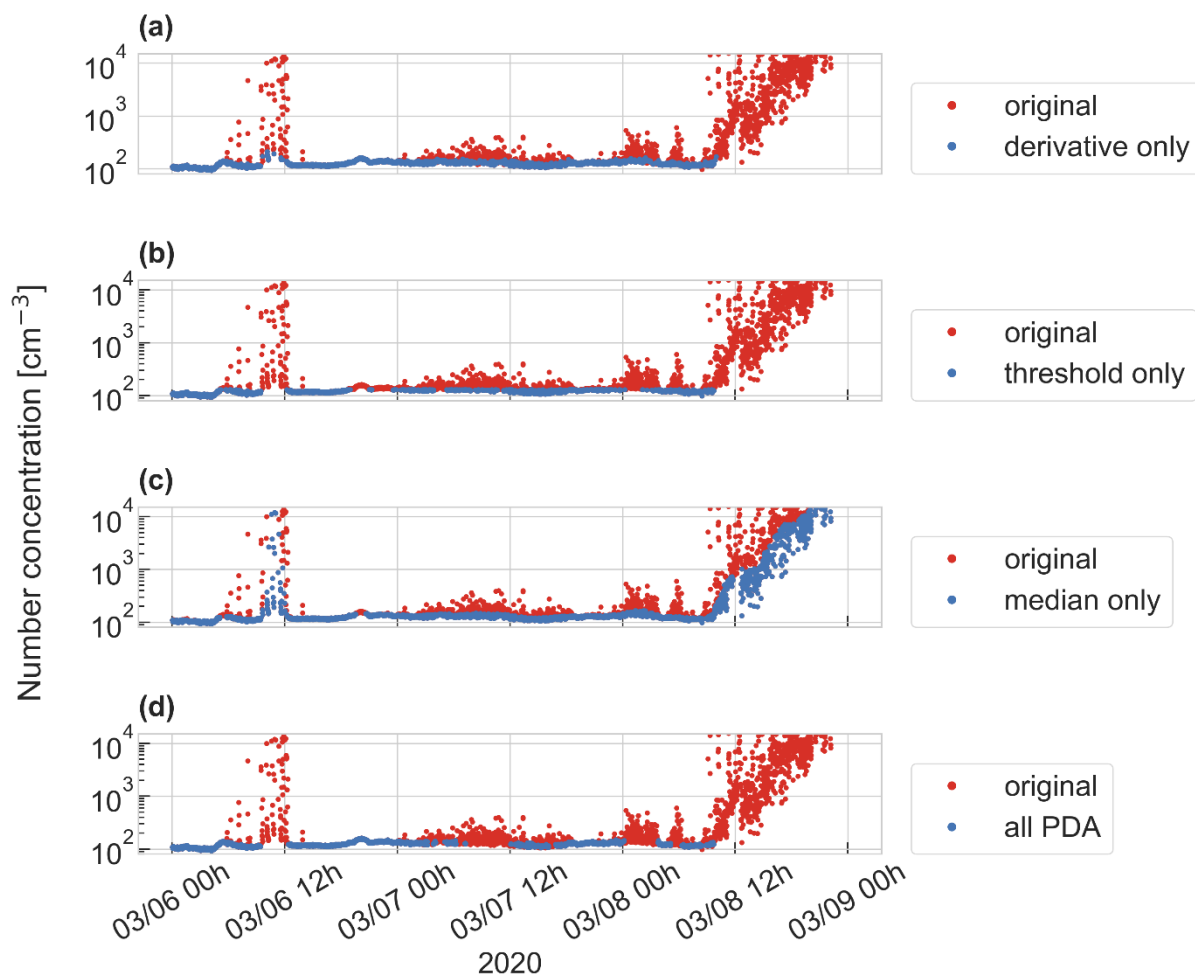
Figure B1: Intercomparison of individual filtering steps on a case study of March 6 to 8. Clean data (in blue) is overlaid over the original data (in Red) after the application of one filtering step individually to the data: a: derivative filter. b: threshold filter. c: median filter. d: All filtering steps of the PDA were applied. For all plots we used data from the CPC3025 at 1 min time resolution. Original data have only been pre-cleaned for zero filter measurements.

Table B1: Percentage of data declared as unaffected when different filtering steps are applied and the mean concentrations and standard deviations of the corresponding particle number concentrations.

Comparison of single filters	Parameters	Remaining data	Mean concentration [cm^{-3}]	Sdandard deviation
Total counts		100%	5198	14598
Derivative filter only	a = 0.5 , m= 0.55	43%	202	618
Threshold filter only	Threshold = 130 cm^{-3}	23%	70	37
Median filter only	Median time = 360 min , median factor = 1.05	68%	2979	10646

43

Derivative and threshold filter	As in Tab. 1	43%	198	244
Derivative, threshold and neighbors filter	As in Tab. 1	39%	191	221
All PDA	As in Tab. 1	38%	191	214

Since local contamination often shows in fast changing concentration spikes, it is worth exploring whether a low-pass filter is applicable. For this, we looked at the power spectral density of the CPC3025 particle concentration data by means of a Fourier frequency decomposition (Fig.B2). No high frequency is visible which would allow a low-pass filter to be applied. Local contamination in this dataset does not show in a high-frequency signal, which is distinguishable from the background signal. The detection of pollution based on frequency analysis is therefore not possible here.
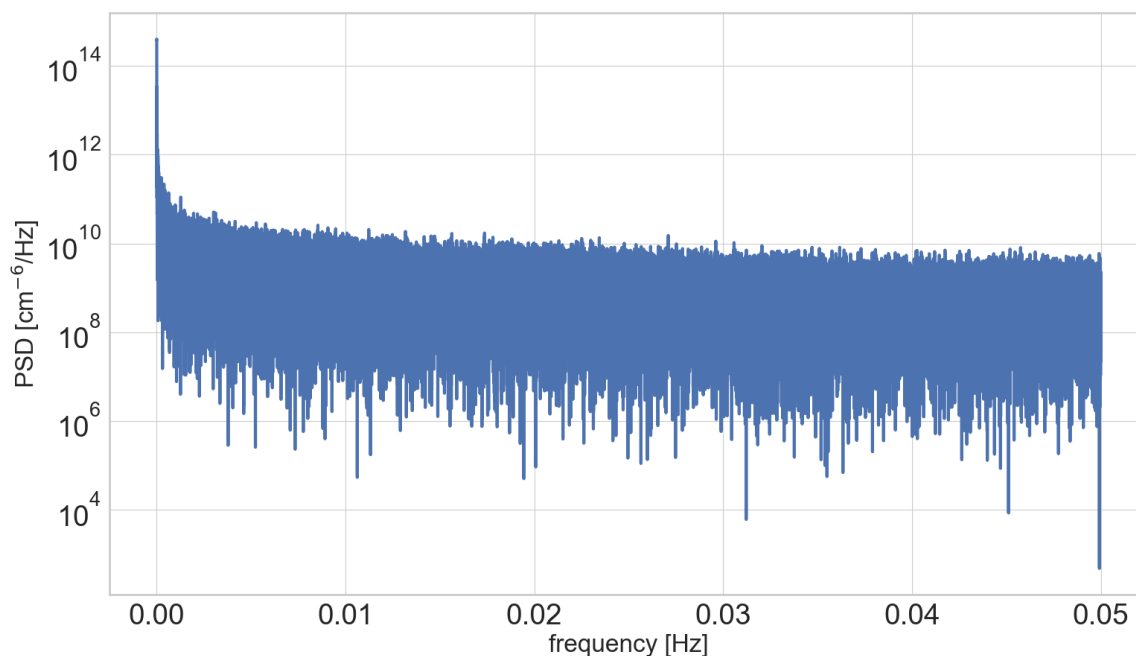
Figure B2: Power spectral density (PSD) of the particle number concentrations of the CPC3025 as a function of the frequencies. The dataset has a time resolution of 10 seconds. For this figure we used the subset of the month March.

In order to elaborate on the effect of changes in the parameters of individual filtering steps, we let the PDA run several times and thereby only change one parameter at the time. The resulting size of the filtered dataset is shown in Table B2. The first row shows the initial setting, as we used them in Table 1. For example, the largest change is caused by turning off the neighbors filter. This increases the dataset by 11.4%. Relatively small changes in the power law slope and intercept of the derivative

44

filter change the size of the dataset by roughly 5-10 %, whereby the effect of changes of the slope are stronger. Changes in the median filter only cause small changes by < 1% to the final dataset. And setting the sparse threshold from 24 to 18 out of 30 data points (from 80% to 60% allowed polluted data points in the sparse window) reduces the dataset by ca. 3%. The table illustrates again that the derivative filter is responsible for the largest part of the filtering by the PDA. Even though the filtering steps 2 to 4 only contribute little to the PDA, they are valuable to avoid false negatives after the application of the derivative filter.

Table B2: The effect of changes in the parameters of individual filtering steps on the number of unaffected data points. The first row shows the standard settings used to filter the CPC3025 dataset and the number of remaining data points. The following rows show changes in different parameters and again the number of unaffected data points with these changes in the PDA.

Initial parameters of the PDA	# Data points after application of PDA	Percentage
a= 0.5 cm^{-3}s^{-1} m= 0.55 s^{-1} lower threshold = 60 cm^{-3} median time interval = 30 min median deviation factor = 1.4 sparse window = 30 sparse threshold = 24	190358	100.0%
Changed parameter		
a= 0.45 cm^{-3}s^{-1}	184297	96.8%
a = 0.6 cm^{-3}s^{-1}	198733	104.4%
m = 0.5 s^{-1}	171060	89.9%
m = 0.6 s^{-1}	202292	106.3%
lower threshold = 100 cm^{-3}	196471	103.2%
median time interval = 120 min	188503	99.0%
median_factor = 1.8	191316	100.5%
median_factor = 5	191893	100.8%
sparse_threshold = 18	185578	97.5%
sparse_threshold = 27	192761	101.3%

45

| no neighbors filter | | 212073 | 111.4% |
| no sparse filter | | 193680 | 101.7% |

## Appendix ~~B~~C: Application of the PDA to various time-resolutions

We use the averaged time series from the ~~gradient~~derivative filter for further filtering steps in the PDA. This comes with the trade-off that the dataset loses time resolution when applying the PDA. In many applications this might not be a problem since data are often collected in higher time resolutions than needed for further analysis. We applied the PDA to the original dataset of the CPC 3025 (10 s time resolution). Figure ~~B1a~~C1a shows the ~~gradient~~derivatives plotted against the total number

895 concentrations for this dataset, which is used to determine the separation line (in red) for the ~~gradient~~derivative filter. It is less intuitive to find a good position of the separation line, compared to the one-minute averaged ~~gradient~~derivative (Fig. 3) because the two branches do not separate as clearly. We chose a separation line with the parameters a = 0.6 cm^{-3}s^{-1} and m = 0.44 s^{-1}. Figure ~~B1b~~C1b shows the same graph for the 10 min averaged time series of the same dataset. Here, we used a = 1 cm^{-3}s^{-1} and m = 0.49 s^{-1} for the separation line. In both cases, it is possible to distinguish between the two ~~gradient~~derivative branches,

900 which indicates polluted and unaffected data. We observe that the separation line tends to go to higher ~~gradient~~derivatives with coarser time resolution, which is a result of the longer averaging time, because this smoothens the variability. Figure ~~B2~~C2 shows the original (in red) and filtered (in blue) time series over three days after application of all PDA filtering steps to the two datasets (10 sec time resolution in panel a, and 10 min time resolution in panel b). The used parameters of the PDA are listed in table ~~B1~~C1. The PDA detects the polluted spikes in both cases and is able to separate clean from polluted data. Even

905 though the lower time resolution data do not have as distinct pollution "spikes". Potential outliers could have been smoothened when averaging. We conclude, the possibility to "tune" different parameters of the PDA makes it applicable to datasets with different temporal resolutions.

Table ~~B1~~C1: Parameters used for the application of the PDA to two datasets with different time resolutions

Filter step	Parameter	Particle number concentration in 10 sec time resolution	Particle number concentration in 10 min time resolution
1A. ~~Gradient~~Derivative filter (Power law)	a m	0.6 cm^{-3}s^{-1} 0.44 s^{-1}	1 cm^{-3}s^{-1} 0.49 s^{-1}
2. Threshold filter	Upper threshold Lower threshold	10^4 cm^{-3} 60 cm^{-3}	10^4 cm^{-3} 60 cm^{-3}
3. Neighboring points filter	On/off	On	On

46

4. Median filter	Median time window	30 min	60 min
	Median deviation factor	1.4	1.4
5. Sparse data filter (no. of data points)	Sparse window	180	12
	Sparse threshold	144	10

910
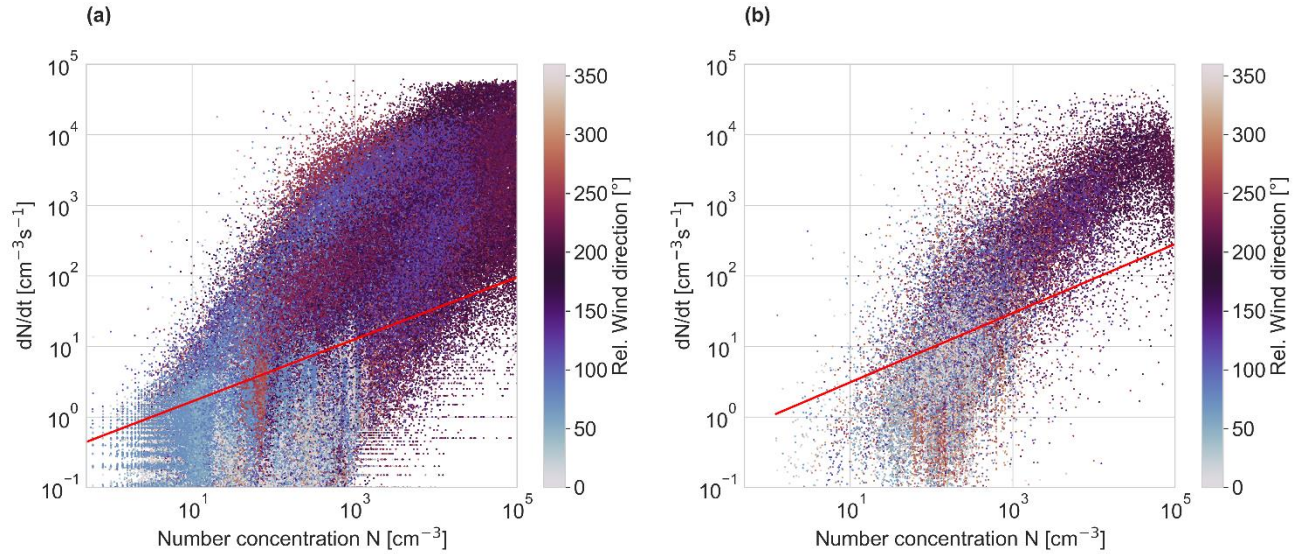
Figure B1C1. Relation of the absolute value of the particle number concentration gradientderivative to the absolute number concentration for two different time resolutions. a: 10 sec, b: 10 min. The color-code indicates the relative wind direction. The red lines separate polluted from unaffected data points with a slope of 0.44 s^{-1} and an intercept of 0.6 cm^{-3}s^{-1} in panel a and a slope of 0.49 s^{-1} and an intercept of 1 cm^{-3}s^{-1} in panel b.

915
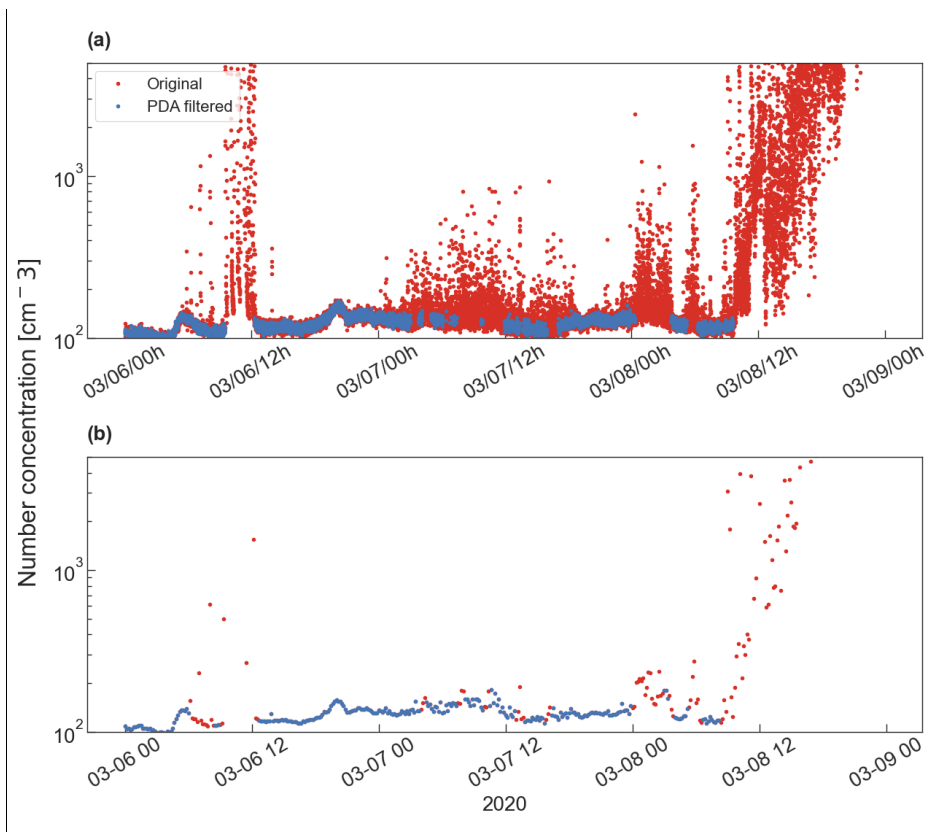
Figure B2C2: Performance test of the PDA on datasets with two different time resolutions. a) 10 sec time resolution data b) 10 min time resolution data. Filtered data in blue is shown on top of the original data of the corresponding time series in red.

Code availability

920   The pollution mask code is available via zenodo (https://doi.org/10.5281/zenodo.5761101).

Data availability

All *Swiss Container* MOSAiC data will be publicly accessible from 1 January 2023 via PANGAEA. Datasets of the raw and the corrected particle number concentrations in 10s time resolution of the CPC 3025 were submitted to PANGAEA on December 6, 2021. A one minute averaged dataset of the CPC 3025, together with a pollution flag created by the PDA was

925   submitted to PANGAEA on December 6, 2021. The ARM datasets are available via the ARM Data Discovery tool: https://adc.arm.gov/discovery/#/ (Kuang et al., 2021). The Jungfraujoch data are available via ebas.nilu.no.

Author contributions

A.B. and I.B. developed the PDA. J.S. and H.A. conceived the manuscript idea. X.G. performed the visual data cleaning. L.D. provided AMS dataset, H.A. provided the trace gases datasets. N.B. and M.G.-B. provided the JFJ data. L.Q., I.B., J.S., T.J., T.L., H.A., M.B. performed measurements on board. I.B., H.A., J.S. wrote the manuscript. All authors commented on the manuscript.

Competing of Interest

The authors declare no conflict of interest.

Acknowledgements

References

Alfred-Wegener-Institut Helmholtz-Zentrum für Polar- und Meeresforschung: Polar Research and Supply Vessel POLARSTERN Operated by the Alfred-Wegener-Institute, Journal of large-scale research facilities, 3, 119, https://doi.org/10.17815/jlsrf-3-163, 2017.

Alroe, J., Cravigan, L. T., Miljevic, B., Johnson, G. R., Selleck, P., Humphries, R. S., Keywood, M. D., Chambers, S. D., Williams, A. G., and Ristovski, Z. D.: Marine productivity and synoptic meteorology drive summer-time variability in Southern Ocean aerosols, Atmos. Chem. Phys., 20, 8047–8062, 965 https://doi.org/10.5194/acp-20-8047-2020, 2020.

Angot, H., Blomquist, B., Howard, D., Archer, S. D., Bariteau, L., Beck, I., Boyer, M., Brasseur, Z., Helmig, D., Hueber, J., Jacobi, H.-W., Jokinen, T., Laurila, T., Posman, K., Quéléver, L. L. J., Shupe, M. D., and Schmale, J.: Year-round trace gas measurements in the Central Arctic during the MOSAiC expedition, submission to Scientific Data, MOSAiC special issue, in prep.

970 Asmi, A., Collaud Coen, M., Ogren, J. A., Andrews, E., Sheridan, P., Jefferson, A., Weingartner, E., Baltensperger, U., Bukowiecki, N., Lihavainen, H., Kivekäs, N., Asmi, E., Aalto, P. P., Kulmala, M., Wiedensohler, A., Birmili, W., Hamed, A., O'Dowd, C., G Jennings, S., Weller, R., Flentje, H., Fjaeraa, A. M., Fiebig, M., Myhre, C. L., Hallar, A. G., Swietlicki, E., Kristensson, A., and Laj, P.: Aerosol decadal trends – Part 2: In-situ aerosol particle number concentrations at GAW and ACTRIS stations, Atmos. 975 Chem. Phys., 13, 895–916, https://doi.org/10.5194/acp-13-895-2013, 2013.

Asmi, E., Kondratyev, V., Brus, D., Laurila, T., Lihavainen, H., Backman, J., Vakkari, V., Aurela, M., Hatakka, J., Viisanen, Y., Uttal, T., Ivakhov, V., and Makshtas, A.: Aerosol size distribution seasonal characteristics measured in Tiksi, Russian Arctic, Atmos. Chem. Phys., 16, 1271–1287, https://doi.org/10.5194/acp-16-1271-2016, 2016.

980 Baccarini, A.: Investigation of New Aerosol Particle Formation in Polar Regions, Doctoral Thesis, ETH Zurich, https://doi.org/10.3929/ethz-b-000502951, 2021.

Baccarini, A., Karlsson, L., Dommen, J., Duplessis, P., Vüllers, J., Brooks, I. M., Saiz-Lopez, A., Salter, M., Tjernström, M., Baltensperger, U., Zieger, P., and Schmale, J.: Frequent new particle formation over the high Arctic pack ice by enhanced iodine emissions, Nat. Commun., 11, 4924, 985 https://doi.org/10.1038/s41467-020-18551-0, 2020.

Beck, L. J., Sarnela, N., Junninen, H., Hoppe, C. J. M., Garmash, O., Bianchi, F., Riva, M., Rose, C., Peräkylä, O., Wimmer, D., Kausiala, O., Jokinen, T., Ahonen, L., Mikkilä, J., Hakala, J., He, X.-C., Kontkanen, J., Wolf, K. K. E., Cappelletti, D., Mazzola, M., Traversi, R., Petroselli, C., Viola, A. P., Vitale, V., Lange, R., Massling, A., Nøjgaard, J. K., Krejci, R., Karlsson, L., Zieger, P., Jang, S., Lee, K., 990 Vakkari, V., Lampilahti, J., Thakur, R. C., Leino, K., Kangasluoma, J., Duplissy, E.-M., Siivola, E., Marbouti, M., Tham, Y. J., Saiz-Lopez, A., Petäjä, T., Ehn, M., Worsnop, D. R., Skov, H., Kulmala, M., Kerminen, V.-M., and Sipilä, M.: Differing Mechanisms of New Particle Formation at Two Arctic Sites, Geophys. Res. Lett., 48, e2020GL091334, https://doi.org/10.1029/2020GL091334, 2021.

Brantley, H. L., Hagler, G. S. W., Kimbrough, E. S., Williams, R. W., Mukerjee, S., and Neas, L. M.: 995 Mobile air monitoring data-processing strategies and effects on spatial air pollution trends, Atmos. Meas. Tech., 7, 2169–2183, https://doi.org/10.5194/amt-7-2169-2014, 2014.

Bukowiecki, N., Dommen, J., Prévôt, A. S. H., Richter, R., Weingartner, E., and Baltensperger, U.: A mobile pollutant measurement laboratory—measuring gas phase and aerosol ambient concentrations with high spatial and temporal resolution, Atmos. Environ., 36, 5569–5579, https://doi.org/10.1016/S1352-2310(02)00694-5, 2002.

Bukowiecki, N., Weingartner, E., Gysel, M., Collaud Coen, M., Zieger, P., Herrmann, E., Steinbacher, M., Gäggeler, H. W., and Baltensperger, U.: A review of more than 20 years of aerosol observation at the high altitude research station Jungfraujoch, Switzerland (3580 m asl), Aerosol Air Qual. Res., 16, 764–788, https://doi.org/10.4209/aaqr.2015.05.0305, 2016.

Bukowiecki, N., Brem, B. T., Wehrle, G., Močnik, G., Affolter, S., Leuenberger, M., Coen, M. C., Hervo, M., Baltensperger, U., and Gysel-Beer, M.: Elucidating local pollution and site representativeness at the Jungfraujoch, Switzerland through parallel aerosol measurements at an adjacent mountain ridge, Environmental Research Communications, 3, 021001, https://doi.org/10.1088/2515-7620/abe987, 2021.

Carslaw, K. S., Boucher, O., Spracklen, D. V., Mann, G. W., Rae, J. G. L., Woodward, S., and Kulmala, M.: A review of natural aerosol interactions and feedbacks within the Earth system, Atmos. Chem. Phys., 10, 1701–1737, https://doi.org/10.5194/acp-10-1701-2010, 2010.

Cox, M. L., Sturrock, G. A., Fraser, P. J., Siems, S. T., Krummel, P. B., and O'Doherty, S.: Regional Sources of Methyl Chloride, Chloroform and Dichloromethane Identified from AGAGE Observations at Cape Grim, Tasmania, 1998–2000, J. Atmos. Chem., 45, 79–99, https://doi.org/10.1023/A:1024022320985, 2003.

Dada, L., Beck, I., Quéléver, L. L. J., Baccarini, A., Angot, H., Laurila, T., Brasseur, Z., Boyer, M., Jozef, G., De Boer, G., Henning, S., Daellenbach, K. R., Jokinen, T., and Schmale, J.: A central Arctic extreme aerosol even triggered by a warm air mass intrusion, in prepNat. Comm., under review.

DeCarlo, P. F., Kimmel, J. R., Trimborn, A., Northway, M. J., Jayne, J. T., Aiken, A. C., Gonin, M., Fuhrer, K., Horvath, T., Docherty, K. S., Worsnop, D. R., and Jimenez, J. L.: Field-Deployable, High-Resolution, Time-of-Flight Aerosol Mass Spectrometer, Anal. Chem., 78, 8281–8289, https://doi.org/10.1021/ac061249n, 2006.

Drewnick, F., Böttger, T., von der Weiden-Reinmüller, S.-L., Zorn, S. R., Klimach, T., Schneider, J., and Borrmann, S.: Design of a mobile aerosol research laboratory and data processing tools for effective stationary and mobile field measurements, Atmos. Meas. Tech., 5, 1443–1457, https://doi.org/10.5194/amt-5-1443-2012, 2012.

El Yazidi, A., Ramonet, M., Ciais, P., Broquet, G., Pison, I., Abbaris, A., Brunner, D., Conil, S., Delmotte, M., Gheusi, F., Guerin, F., Hazan, L., Kachroudi, N., Kouvarakis, G., Mihalopoulos, N., Rivier, L., and Serça, D.: Identification of spikes associated with local sources in continuous time series of atmospheric

CO, CO_2 and CH_4, Atmos. Meas. Tech., 11, 1599–1614, https://doi.org/10.5194/amt-11-1599-2018, 2018.

Enroth, J., Saarikoski, S., Niemi, J., Kousa, A., Ježek, I., Močnik, G., Carbone, S., Kuuluvainen, H., Rönkkö, T., Hillamo, R., and Pirjola, L.: Chemical and physical characterization of traffic particles in four different highway environments in the Helsinki metropolitan area, Atmos. Chem. Phys., 16, 5497–5512, https://doi.org/10.5194/acp-16-5497-2016, 2016.

Enroth, J., Kangasluoma, J., Korhonen, F., Hering, S., Picard, D., Lewis, G., Attoui, M., and Petäjä, T.: On the time response determination of condensation particle counters, Aerosol Sci. Tech., 52, 778–787, https://doi.org/10.1080/02786826.2018.1460458, 2018.

Fontijn, A., Sabadell, A. J., and Ronco, R. J.: Homogeneous chemiluminescent measurement of nitric oxide with ozone. Implications for continuous selective monitoring of gaseous air pollutants, Anal. Chem., 42, 575–579, https://doi.org/10.1021/ac60288a034, 1970.

Freud, E., Krejci, R., Tunved, P., Leaitch, R., Nguyen, Q. T., Massling, A., Skov, H., and Barrie, L.: Pan-Arctic aerosol number size distributions: seasonality and transport patterns, Atmos. Chem. Phys., 17, 8101–8128, https://doi.org/10.5194/acp-17-8101-2017, 2017.

Frossard, A. A., Russell, L. M., Burrows, S. M., Elliott, S. M., Bates, T. S., and Quinn, P. K.: Sources and composition of submicron organic mass in marine aerosol particles: Marine Aerosol Organic Mass Composition, J. Geophys. Res. Atmos., 119, 12,977-13,003, https://doi.org/10.1002/2014JD021913, 2014.

Gallo, F., Uin, J., Springston, S., Wang, J., Zheng, G., Kuang, C., Wood, R., Azevedo, E. B., McComiskey, A., Mei, F., Theisen, A., Kyrouac, J., and Aiken, A. C.: Identifying a regional aerosol baseline in the eastern North Atlantic using collocated measurements and a mathematical algorithm to mask high-submicron-number-concentration aerosol events, Atmos. Chem. Phys., 20, 7553–7573, https://doi.org/10.5194/acp-20-7553-2020, 2020.

Giostra, U., Furlani, F., Arduini, J., Cava, D., Manning, A. J., O'Doherty, S. J., Reimann, S., and Maione, M.: The determination of a "regional" atmospheric background mixing ratio for anthropogenic greenhouse gases: A comparison of two independent methods, Atmos. Environ., 45, 7396–7405, https://doi.org/10.1016/j.atmosenv.2011.06.076, 2011.

Hagler, G. S. W., Lin, M.-Y., Khlystov, A., Baldauf, R. W., Isakov, V., Faircloth, J., and Jackson, L. E.: Field investigation of roadside vegetative and structural barrier impact on near-road ultrafine particle concentrations under a variety of wind conditions, Science of The Total Environment, 419, 7–15, https://doi.org/10.1016/j.scitotenv.2011.12.002, 2012.

Herrmann, E., Weingartner, E., Henne, S., Vuilleumier, L., Bukowiecki, N., Steinbacher, M., Conen, F., Collaud Coen, M., Hammer, E., Jurányi, Z., Baltensperger, U., and Gysel, M.: Analysis of long-term

1065 aerosol size distribution data from Jungfraujoch with emphasis on free tropospheric conditions, cloud influence, and air mass transport, J. Geophys. Res. Atmos., 120, 9459–9480, https://doi.org/10.1002/2015JD023660, 2015.

Humphries, R. S., Klekociuk, A. R., Schofield, R., Keywood, M., Ward, J., and Wilson, S. R.: Unexpectedly high ultrafine aerosol concentrations above East Antarctic sea ice, Atmos. Chem. Phys.,
1070 16, 2185–2206, https://doi.org/10.5194/acp-16-2185-2016, 2016.

Humphries, R. S., McRobert, I. M., Ponsonby, W. A., Ward, J. P., Keywood, M. D., Loh, Z. M., Krummel, P. B., and Harnwell, J.: Identification of platform exhaust on the RV Investigator, Atmos. Meas. Tech., 12, 3019–3038, https://doi.org/10.5194/amt-12-3019-2019, 2019.

Kolesar, K. R., Cellini, J., Peterson, P. K., Jefferson, A., Tuch, T., Birmili, W., Wiedensohler, A., and
1075 Pratt, K. A.: Effect of Prudhoe Bay emissions on atmospheric aerosol growth events observed in Utqiaġvik (Barrow), Alaska, Atmos. Environ., 152, 146–155, https://doi.org/10.1016/j.atmosenv.2016.12.019, 2017.

Kuang, C., Salwen, C., Boyer, M., and Singh, A.: Condensation Particle Counter (AOSCPCF), Atmospheric Radiation Measurement (ARM) user facility, 2021. https://doi.org/10.5439/1046184,
1080 Accessed December 6.

Kulmala, M., Petäjä, T., Ehn, M., Thornton, J., Sipilä, M., Worsnop, D. r., and Kerminen, V.-M.: Chemistry of Atmospheric Nucleation: On the Recent Advances on Precursor Characterization and Atmospheric Cluster Composition in Connection with Atmospheric New Particle Formation, Annu. Rev. Phys. Chem., 65, 21–37, https://doi.org/10.1146/annurev-physchem-040412-110014, 2014.

1085 Kyrö, E.-M., Kerminen, V.-M., Virkkula, A., Dal Maso, M., Parshintsev, J., Ruíz-Jimenez, J., Forsström, L., Manninen, H. E., Riekkola, M.-L., Heinonen, P., and Kulmala, M.: Antarctic new particle formation from continental biogenic precursors, Atmos. Chem. Phys., 13, 3527–3546, https://doi.org/10.5194/acp-13-3527-2013, 2013.

Leck, C., Bigg, E. K., Covert, D. S., Heintzenberg, J., Maenhaut, W., Nilsson, E. D., and Wiedensohler,
1090 A.: Overview of the atmospheric research program during the International Arctic Ocean Expedition of 1991 (IAOE-91) and its scientific results, Tellus B: Chemical and Physical Meteorology, 48, 136–155, https://doi.org/10.3402/tellusb.v48i2.15833, 1996.

Liu, J., Dedrick, J., Russell, L. M., Senum, G. I., Uin, J., Kuang, C., Springston, S. R., Leaitch, W. R., Aiken, A. C., and Lubin, D.: High summertime aerosol organic functional group concentrations from
1095 marine and seabird sources at Ross Island, Antarctica, during AWARE, Atmos. Chem. Phys., 18, 8571–8587, https://doi.org/10.5194/acp-18-8571-2018, 2018.

Maslanik, J. and Stroeve, J.: Near-Real-Time DMSP SSMIS Daily Polar Gridded Sea Ice Concentrations, Version 1, September 2019, Boulder, Colorado USA. NASA National Snow and Ice Date Center

Distributed Active Archive Center., https://doi.org/10.5067/U8C09DWVX9LM, 1999. Accessed in August 2021.

Massoli, P., Fortner, E. C., Canagaratna, M. R., Williams, L. R., Zhang, Q., Sun, Y., Schwab, J. J., Trimborn, A., Onasch, T. B., Demerjian, K. L., Kolb, C. E., Worsnop, D. R., and Jayne, J. T.: Pollution Gradients and Chemical Characterization of Particulate Matter from Vehicular Traffic near Major Roadways: Results from the 2009 Queens College Air Quality Study in NYC, Aerosol Sci. Tech., 46, 1201–1218, https://doi.org/10.1080/02786826.2012.701784, 2012.

McFarquhar, G. M., Bretherton, C. S., Marchand, R., Protat, A., DeMott, P. J., Alexander, S. P., Roberts, G. C., Twohy, C. H., Toohey, D., Siems, S., Huang, Y., Wood, R., Rauber, R. M., Lasher-Trapp, S., Jensen, J., Stith, J. L., Mace, J., Um, J., Järvinen, E., Schnaiter, M., Gettelman, A., Sanchez, K. J., McCluskey, C. S., Russell, L. M., McCoy, I. L., Atlas, R. L., Bardeen, C. G., Moore, K. A., Hill, T. C. J., Humphries, R. S., Keywood, M. D., Ristovski, Z., Cravigan, L., Schofield, R., Fairall, C., Mallet, M. D., Kreidenweis, S. M., Rainwater, B., D'Alessandro, J., Wang, Y., Wu, W., Saliba, G., Levin, E. J. T., Ding, S., Lang, F., Truong, S. C. H., Wolff, C., Haggerty, J., Harvey, M. J., Klekociuk, A. R., and McDonald, A.: Observations of Clouds, Aerosols, Precipitation, and Surface Radiation over the Southern Ocean: An Overview of CAPRICORN, MARCUS, MICRE, and SOCRATES, B. Am. Meteorol. Soc., 102, E894–E928, https://doi.org/10.1175/BAMS-D-20-0132.1, 2021.

Moallemi, A., Landwehr, S., Robinson, C., Simó, R., Zamanillo, M., Chen, G., Baccarini, A., Schnaiter, M., Henning, S., Modini, R. L., Gysel-Beer, M., and Schmale, J.: Sources, Occurrence and Characteristics of Fluorescent Biological Aerosol Particles Measured Over the Pristine Southern Ocean, J. Geophys. Res. Atmos., 126, e2021JD034811, https://doi.org/10.1029/2021JD034811, 2021.

McNabola, A., McCreddin, A., Gill, L. W., and Broderick, B. M.: Analysis of the relationship between urban background air pollution concentrations and the personal exposure of office workers in Dublin, Ireland, using baseline separation techniques, Atmospheric Pollution Research, 2, 80–88, https://doi.org/10.5094/APR.2011.010, 2011.

Nixdorf, U., Dethloff, K., Rex, M., Shupe, M., Sommerfeld, A., Perovich, D. K., Nicolaus, M., Heuzé, C., Rabe, B., Loose, B., Damm, E., Gradinger, R., Fong, A., Maslowski, W., Rinke, A., Kwok, R., Spreen, G., Wendisch, M., Herber, A., Hirsekorn, M., Mohaupt, V., Frickenhaus, S., Immerz, A., Weiss-Tuider, K., König, B., Mengedoht, D., Regnery, J., Gerchow, P., Ransby, D., Krumpen, T., Morgenstern, A., Haas, C., Kanzow, T., Rack, F. R., Saitzev, V., Sokolov, V., Makarov, A., Schwarze, S., Wunderlich, T., Wurr, K., and Boetius, A.: MOSAiC Extended Acknowledgement, https://doi.org/10.5281/zenodo.5541624, 2021.

Reddington, C. L., Carslaw, K. S., Stier, P., Schutgens, N., Coe, H., Liu, D., Allan, J., Browse, J., Pringle, K. J., Lee, L. A., Yoshioka, M., Johnson, J. S., Regayre, L. A., Spracklen, D. V., Mann, G. W., Clarke, A., Hermann, M., Henning, S., Wex, H., Kristensen, T. B., Leaitch, W. R., Pöschl, U., Rose, D., Andreae, M. O., Schmale, J., Kondo, Y., Oshima, N., Schwarz, J. P., Nenes, A., Anderson, B., Roberts, G. C., Snider, J. R., Leck, C., Quinn, P. K., Chi, X., Ding, A., Jimenez, J. L., and Zhang, Q.: The Global Aerosol

Synthesis and Science Project (GASSP): Measurements and Modeling to Reduce Uncertainty, B. Am. Meteorol. Soc., 98, 1857–1877, https://doi.org/10.1175/BAMS-D-15-00317.1, 2017.

Ruckstuhl, A. F., Henne, S., Reimann, S., Steinbacher, M., Vollmer, M. K., O'Doherty, S., Buchmann, B., and Hueglin, C.: Robust extraction of baseline signal of atmospheric trace species using local regression, Atmos. Meas. Tech., 5, 2613–2624, https://doi.org/10.5194/amt-5-2613-2012, 2012.

Schmale, J. and Baccarini, A.: Progress in Unraveling Atmospheric New Particle Formation and Growth Across the Arctic, Geophys. Res. Lett., 48, e2021GL094198, https://doi.org/10.1029/2021GL094198, 2021.

Schmale, J., Schneider, J., Nemitz, E., Tang, Y. S., Dragosits, U., Blackall, T. D., Trathan, P. N., Phillips, G. J., Sutton, M., and Braban, C. F.: Sub-Antarctic marine aerosol: dominant contributions from biogenic sources, Atmos. Chem. Phys., 13, 8669–8694, https://doi.org/10.5194/acp-13-8669-2013, 2013.

Schmale, J., Henning, S., Henzing, B., Keskinen, H., Sellegri, K., Ovadnevaite, J., Bougiatioti, A., Kalivitis, N., Stavroulas, I., Jefferson, A., Park, M., Schlag, P., Kristensson, A., Iwamoto, Y., Pringle, K., Reddington, C., Aalto, P., Äijälä, M., Baltensperger, U., Bialek, J., Birmili, W., Bukowiecki, N., Ehn, M., Fjæraa, A. M., Fiebig, M., Frank, G., Fröhlich, R., Frumau, A., Furuya, M., Hammer, E., Heikkinen, L., Herrmann, E., Holzinger, R., Hyono, H., Kanakidou, M., Kiendler-Scharr, A., Kinouchi, K., Kos, G., Kulmala, M., Mihalopoulos, N., Motos, G., Nenes, A., O'Dowd, C., Paramonov, M., Petäjä, T., Picard, D., Poulain, L., Prévôt, A. S. H., Slowik, J., Sonntag, A., Swietlicki, E., Svenningsson, B., Tsurumaru, H., Wiedensohler, A., Wittbom, C., Ogren, J. A., Matsuki, A., Yum, S. S., Myhre, C. L., Carslaw, K., Stratmann, F., and Gysel, M.: Collocated observations of cloud condensation nuclei, particle size distributions, and chemical composition, Sci. Data, 4, 170003, https://doi.org/10.1038/sdata.2017.3, 2017.

Schmale, J., Henning, S., Decesari, S., Henzing, B., Keskinen, H., Sellegri, K., Ovadnevaite, J., Pöhlker, M. L., Brito, J., Bougiatioti, A., Kristensson, A., Kalivitis, N., Stavroulas, I., Carbone, S., Jefferson, A., Park, M., Schlag, P., Iwamoto, Y., Aalto, P., Äijälä, M., Bukowiecki, N., Ehn, M., Frank, G., Fröhlich, R., Frumau, A., Herrmann, E., Herrmann, H., Holzinger, R., Kos, G., Kulmala, M., Mihalopoulos, N., Nenes, A., O'Dowd, C., Petäjä, T., Picard, D., Pöhlker, C., Pöschl, U., Poulain, L., Prévôt, A. S. H., Swietlicki, E., Andreae, M. O., Artaxo, P., Wiedensohler, A., Ogren, J., Matsuki, A., Yum, S. S., Stratmann, F., Baltensperger, U., and Gysel, M.: Long-term cloud condensation nuclei number concentration, particle number size distribution and chemical composition measurements at regionally representative observatories, Atmos. Chem. Phys., 18, 2853–2881, https://doi.org/10.5194/acp-18-2853-2018, 2018.

Schmale, J., Baccarini, A., Thurnherr, I., Henning, S., Efraim, A., Regayre, L., Bolas, C., Hartmann, M., Welti, A., Lehtipalo, K., Aemisegger, F., Tatzelt, C., Landwehr, S., Modini, R. L., Tummon, F., Johnson, J. S., Harris, N., Schnaiter, M., Toffoli, A., Derkani, M., Bukowiecki, N., Stratmann, F., Dommen, J., Baltensperger, U., Wernli, H., Rosenfeld, D., Gysel-Beer, M., and Carslaw, K. S.: Overview of the Antarctic Circumnavigation Expedition: Study of Preindustrial-like Aerosols and Their Climate Effects

(ACE-SPACE), B. Am. Meteorol. Soc., 100, 2260–2283, https://doi.org/10.1175/BAMS-D-18-0187.1, 2019.

1175 Schmithuesen, H.: Continuous meteorological surface measurement during POLARSTERN cruise PS122/1, Alfred Wegener Institute, Helmholtz Centre for Polar and Marine Research, Bremerhaven, PANGAEA, https://doi.org/10.1594/PANGAEA.935221, 23 August 2021a.

Schmithuesen, H.: Continuous meteorological surface measurement during POLARSTERN cruise PS122/2, Alfred Wegener Institute, Helmholtz Centre for Polar and Marine Research, Bremerhaven, 1180 PANGAEA, https://doi.org/10.1594/PANGAEA.935222, 23 August 2021b.

Schmithuesen, H.: Continuous meteorological surface measurement during POLARSTERN cruise PS122/3, Alfred Wegener Institute, Helmholtz Centre for Polar and Marine Research, Bremerhaven, PANGAEA, https://doi.org/10.1594/PANGAEA.935223, 23 August 2021c.

Schmithuesen, H.: Continuous meteorological surface measurement during POLARSTERN cruise 1185 PS122/4, Alfred Wegener Institute, Helmholtz Centre for Polar and Marine Research, Bremerhaven, PANGAEA, https://doi.org/10.1594/PANGAEA.935224, 23 August 2021d.

Schmithuesen, H.: Continuous meteorological surface measurement during POLARSTERN cruise PS122/5, Alfred Wegener Institute, Helmholtz Centre for Polar and Marine Research, Bremerhaven, PANGAEA, https://doi.org/10.1594/PANGAEA.935225, 23 August 2021e.

1190 Shupe, M. D., Rex, M., Blomquist, B., Persson, P. O. G., Schmale J., Uttal, T., Althausen, D., Angot, H., Archer, S., Bariteau, L., Beck, I., Bilberry, J., Bucci, S., Buck, C., Boyer, M., Brasseur, Z., Brooks, I. M., Calmer R., Cassano J., Castro V., Chu, D., Costa, D., Cox, C. J., Creamean, J., Crewell, S., Dahlke, S., Damm, E., de Boer, G., Deckelmann, H., Dethloff, K., Dütsch, M., Ebell, K., Ehrlich, A., Ellis, J., Engelmann, R., Fong, A. A., Frey, M. M., Gallagher, M. R., Ganzeveld, L.,Gradinger R., Graeser, J., 1195 Greenamyer, V., Griesche, H., Griffiths, S., Hamilton, J., Heinemann, G., Helmig, D., Herber A., Heuzé C. , Hofer, J., Houchens, T., Howard, D., Inoue J., Jacobi, H. W., , Jaiser, R., Jokinen, T., Jourdan, O., Jozef, G., King, W., Kirchgaessner, A., Klingebiel, M., Krassovski, M., Krumpen, T., Lampert, A., Landing, W., Laurila, T., Lawrence, D., Lonardi, M., Loose, B., Lüpkes, C., Maahn, M., Macke, A., Maslowski, W., Marsay, C., Maturilli, M., Mech, M., Morris, S., Moser, M., Nicolaus, M., Ortega, P., 1200 Osborn, J., Pätzold F., Perovich, D. K., Petäjä, T., Pilz, C., Pirazzini, R., Posman, K., Powers, H., Pratt, K. A., Preußer, A., Quéléver, L., Radenz, M., Rabe, B., Rinke, A., Sachs, T., Schulz, A., Siebert, H., Silva, T., Solomon, A., Sommerfeld, A., Spreen, G., Stephens, M., Stohl, A., Svensson, G., Uin, J., Viegas, J., Voigt, C., von der Gathen, P., Wehner, B., Welker, J. M., Wendisch, M., Werner, M., Xie, Z., and Yue, F.: Overview of the MOSAiC Expedition – Atmosphere, Elementa, 86, under review.

1205 Tjernström, M., Leck, C., Birch, C. E., Bottenheim, J. W., Brooks, B. J., Brooks, I. M., Bäcklin, L., Chang, R. Y.-W., de Leeuw, G., Di Liberto, L., de la Rosa, S., Granath, E., Graus, M., Hansel, A., Heintzenberg, J., Held, A., Hind, A., Johnston, P., Knulst, J., Martin, M., Matrai, P. A., Mauritsen, T., Müller, M., Norris, S. J., Orellana, M. V., Orsini, D. A., Paatero, J., Persson, P. O. G., Gao, Q., Rauschenberg, C., Ristovski,

Z., Sedlar, J., Shupe, M. D., Sierau, B., Sirevaag, A., Sjogren, S., Stetzer, O., Swietlicki, E., Szczodrak, M., Vaattovaara, P., Wahlberg, N., Westberg, M., and Wheeler, C. R.: The Arctic Summer Cloud Ocean Study (ASCOS): overview and experimental design, Atmos. Chem. Phys., 14, 2823–2869, https://doi.org/10.5194/acp-14-2823-2014, 2014.

Uin, J., Aiken, A. C., Dubey, M. K., Kuang, C., Pekour, M., Salwen, C., Sedlacek, A. J., Senum, G., Smith, S., Wang, J., Watson, T. B., and Springston, S. R.: Atmospheric Radiation Measurement (ARM) Aerosol Observing Systems (AOS) for Surface-Based In Situ Atmospheric Aerosol and Trace Gas Measurements, J. Atmos. Ocean. Tech., 36, 2429–2447, https://doi.org/10.1175/JTECH-D-19-0077.1, 2019.

Uttal, T., Curry, J. A., Mcphee, M. G., Perovich, D. K., Moritz, R. E., Maslanik, J. A., Guest, P. S., Stern, H. L., Moore, J. A., Turenne, R., Heiberg, A., Serreze, M. C., Wylie, D. P., Persson, O. G., Paulson, C. A., Halle, C., Morison, J. H., Wheeler, P. A., Makshtas, A., Welch, H., Shupe, M. D., Intrieri, J. M., Stamnes, K., Lindsey, R. W., Pinkel, R., Pegau, W. S., Stanton, T. P., and Grenfeld, T. C.: Surface Heat Budget of the Arctic Ocean, B. Am. Meteorol. Soc., 83, 255–275, https://doi.org/10.1175/1520-0477(2002)083<0255:SHBOTA>2.3.CO;2, 2002.

Uttal, T., Starkweather, S., Drummond, J. R., Vihma, T., Makshtas, A. P., Darby, L. S., Burkhart, J. F., Cox, C. J., Schmeisser, L. N., Haiden, T., Maturilli, M., Shupe, M. D., Boer, G. D., Saha, A., Grachev, A. A., Crepinsek, S. M., Bruhwiler, L., Goodison, B., McArthur, B., Walden, V. P., Dlugokencky, E. J., Persson, P. O. G., Lesins, G., Laurila, T., Ogren, J. A., Stone, R., Long, C. N., Sharma, S., Massling, A., Turner, D. D., Stanitski, D. M., Asmi, E., Aurela, M., Skov, H., Eleftheriadis, K., Virkkula, A., Platt, A., Førland, E. J., Iijima, Y., Nielsen, I. E., Bergin, M. H., Candlish, L., Zimov, N. S., Zimov, S. A., O'Neill, N. T., Fogal, P. F., Kivi, R., Konopleva-Akish, E. A., Verlinde, J., Kustov, V. Y., Vasel, B., Ivakhov, V. M., Viisanen, Y., and Intrieri, J. M.: International Arctic Systems for Observing the Atmosphere: An International Polar Year Legacy Consortium, B. Am. Meteorol. Soc., 97, 1033–1056, https://doi.org/10.1175/bams-d-14-00145.1, 2016.

World Meteorological Organization, World Meteorological Organization, and Global Atmosphere Watch: WMO/GAW aerosol measurement procedures: guidelines and recommendations., WMO/GAW, 2016.